



**HAL**  
open science

## PEGylated Anionic Magneto-Fluorescent Nanoassemblies: Impact of their Interface Structure on MRI Contrast and Cellular Uptake

Camille Linot, Julien Poly, Joanna Boucard, Daniel Pouliquen, Steven Nedellec, Philippe Hulin, Nadège Marec, Paolo Arosio, Alessandro Lascialfari, Andrea Guerrini, et al.

### ► To cite this version:

Camille Linot, Julien Poly, Joanna Boucard, Daniel Pouliquen, Steven Nedellec, et al.. PEGylated Anionic Magneto-Fluorescent Nanoassemblies: Impact of their Interface Structure on MRI Contrast and Cellular Uptake. *ACS Applied Materials & Interfaces*, 2017, 9 (16), pp.14242-14257. 10.1021/ac-sami.7b01737 . inserm-01522631

**HAL Id: inserm-01522631**

**<https://inserm.hal.science/inserm-01522631>**

Submitted on 15 May 2017

**HAL** is a multi-disciplinary open access archive for the deposit and dissemination of scientific research documents, whether they are published or not. The documents may come from teaching and research institutions in France or abroad, or from public or private research centers.

L'archive ouverte pluridisciplinaire **HAL**, est destinée au dépôt et à la diffusion de documents scientifiques de niveau recherche, publiés ou non, émanant des établissements d'enseignement et de recherche français ou étrangers, des laboratoires publics ou privés.



# PEGylated Anionic Magneto-Fluorescent Nanoassemblies: Impact of their Interface Structure on MRI Contrast and Cellular Uptake

Camille Linot, Julien Poly, Joanna Boucard, Daniel Pouliquen, Steven Nedellec, Philippe Hulin, Nadège Marec, Paolo Arosio, Alessandro Lascialfari, Andrea Guerrini, et al.

► **To cite this version:**

Camille Linot, Julien Poly, Joanna Boucard, Daniel Pouliquen, Steven Nedellec, et al.. PEGylated Anionic Magneto-Fluorescent Nanoassemblies: Impact of their Interface Structure on MRI Contrast and Cellular Uptake. ACS Applied Materials & Interfaces, American Chemical Society, 2017, .

**HAL Id: inserm-01522631**

**<http://www.hal.inserm.fr/inserm-01522631>**

Submitted on 15 May 2017

**HAL** is a multi-disciplinary open access archive for the deposit and dissemination of scientific research documents, whether they are published or not. The documents may come from teaching and research institutions in France or abroad, or from public or private research centers.

L'archive ouverte pluridisciplinaire **HAL**, est destinée au dépôt et à la diffusion de documents scientifiques de niveau recherche, publiés ou non, émanant des établissements d'enseignement et de recherche français ou étrangers, des laboratoires publics ou privés.

# PEGylated Anionic Magneto-Fluorescent Nanoassemblies: Impact of their Interface Structure on MRI Contrast and Cellular Uptake

*Camille Linot,<sup>†</sup> Julien Poly,<sup>\*‡</sup> Joanna Boucard,<sup>§</sup> Daniel Pouliquen,<sup>†</sup> Steven Nedellec,<sup>≠</sup> Philippe Hulin,<sup>≠</sup> Nadège Marec,<sup>#</sup> Paolo Arosio,<sup>⊥</sup> Alessandro Lascialfari,<sup>⊥Δ</sup> Andrea Guerrini,<sup>//</sup> Claudio Sangregorio,<sup>//</sup> Marc Lecouvey,<sup>⊥,‡</sup> Lénaïc Lartigue,<sup>§</sup> Christophe Blanquart,<sup>\*†</sup> and Eléna Ishow<sup>\*§</sup>*

<sup>†</sup>CRCINA, INSERM, Université d'Angers, Université de Nantes, Nantes. <sup>‡</sup>IS2M-UMR CNRS 7361, Université de Haute-Alsace, 15 rue Jean Starcky, 68057 Mulhouse, France. <sup>§</sup>CEISAM-UMR CNRS 6230, Université de Nantes, 2 rue de la Houssinière, 44322 Nantes, France. <sup>≠</sup>INSERM UMS 016-UMS CNRS 3556, 8 quai Moncousu, 44007 Nantes, France. <sup>#</sup>Plateforme CytoCell, INSERM UMR 1232, Nantes, France. <sup>⊥</sup>Department of Physics, Università di Pavia, via Bassi, 27100 Pavia, Italy. <sup>Δ</sup>Department of Physics, Università degli Studi di Milano and INSTM, via Celoria 16, 20133 Milano, Italy. <sup>//</sup>ICCOM-CNR, via Madonna del Piano 10, 50019 Sesto Fiorentino, FI, Italy. <sup>⊥</sup>CSPBAT-UMR CNRS 7244, Université de Villetaneuse – Paris 13, 74 rue Marcel Cachin, 93017 Bobigny, France.

**KEYWORDS.** Multimodal nanoassemblies, organic nanoparticles, iron oxide nanoparticles water-soluble RAFT polymers, fluorescence, MRI, live cells, spheroids.

1  
2  
3 **ABSTRACT.** Controlling the interactions of functional nanostructures with water and biological  
4 media represents high challenges in the field of bioimaging applications. Large contrast at low  
5 doses, high colloidal stability in physiological conditions, absence of cell cytotoxicity and  
6 efficient cell internalization represent strong additional needs. To achieve such requirements, we  
7 report on high payload magneto-fluorescent architectures, made of a shell of superparamagnetic  
8 iron oxide nanoparticles tightly anchored around fluorescent organic nanoparticles. Their  
9 external coating is simply modulated using anionic polyelectrolytes in a final step to provide  
10 efficient MRI and fluorescence imaging of live cells. Various structures of pegylated  
11 polyelectrolytes have been synthesized and investigated, differing from their iron oxide  
12 complexing units (carboxylic versus phosphonic acid), their structure (block or comb-like), their  
13 hydrophobicity and their fabrication process (conventional or RAFT-controlled radical  
14 polymerization) while keeping the central magneto-fluorescent platforms the same. Combined  
15 photophysical, magnetic, NMRD and structural investigations proved the superiority of RAFT  
16 polymer coatings containing carboxylate units and a hydrophobic tail to impart the magnetic  
17 nanoassemblies with enhanced-MRI negative contrast, characterized by a high  $r_2/r_1$  ratio and  
18 transverse relaxation  $r_2$  equal to 21 and 125  $\text{s}^{-1}\text{mmol}^{-1}\text{L}$  respectively at 60 MHz clinical  
19 frequency ( $\sim 1.5$  T). Thanks to their dual modality, cell internalization of the nanoassemblies in  
20 mesothelioma cancer cells could be evidenced both by confocal fluorescence microscopy and  
21 magnetophoresis. A 72 h follow-up showed efficient uptake after 24 h with no notable cell  
22 mortality. These studies again pointed out the distinct behavior of RAFT polyelectrolyte-coated  
23 bimodal nanoassemblies that internalize at a slower rate with no adverse cytotoxicity. Extension  
24 to multicellular tumor cell spheroids that mimic solid tumors revealed successful internalization  
25 of the nanoassemblies in the periphery cells, which provides efficient deep-imaging labels thanks  
26  
27  
28  
29  
30  
31  
32  
33  
34  
35  
36  
37  
38  
39  
40  
41  
42  
43  
44  
45  
46  
47  
48  
49  
50  
51  
52  
53  
54  
55  
56  
57  
58  
59  
60

1  
2  
3 to their induced  $T_2^*$  contrast, large emission Stokes shift and bright dot-like signal, popping out  
4  
5 of the strong spheroid autofluorescence.  
6  
7  
8  
9  
10

## 11 12 13 INTRODUCTION

14  
15  
16 Multifunctional nanoassemblies comprising units with complementary properties have emerged  
17  
18 as must-have systems in the field of bioimaging for the last decade.<sup>1-2</sup> They advantageously  
19  
20 enable cross-correlation analyses to avoid false positives and adapt more easily to the location or  
21  
22 the target to be examined, opening the path toward personalized medicine. In this respect,  
23  
24 magneto-fluorescent nanostructures represent attractive multimodal imaging agents that can  
25  
26 bridge the gap between *in vitro* and *in vivo* investigations. They facilitate high-resolution  
27  
28 diagnosis under simple handling and addressing conditions without requiring specific protection  
29  
30 equipment against ionizing radiation.<sup>3-4</sup> Designing complex architectures with high performances  
31  
32 thus represents one big challenge while colloidal and chemical stability, biodegradability as well  
33  
34 as non-significant toxicity represent even higher stakes. For these reasons, superparamagnetic  
35  
36 iron oxide nanoparticles (SPIONs), regarded as non-cytotoxic,<sup>5</sup> have widely been used as  
37  
38 efficient negative contrast agents in magnetic resonance imaging (MRI) thanks to their large  
39  
40 transverse relaxivity  $r_2$ , and their possible biodegradation upon mineralization and sequestration  
41  
42 in iron-loading and transferring proteins.<sup>6-7</sup> Small superparamagnetic magnetite  $Fe_3O_4$  or  
43  
44 maghemite  $\gamma\text{-}Fe_2O_3$  nanoparticles with diameter less than 10 nm have attracted special attention  
45  
46 as they are faster cleared *in vivo* compared to larger nanoparticles.<sup>8-10</sup> To provide higher imaging  
47  
48 contrast, recent interest has been paid to tight clustering of SPIONs within single nanoassemblies  
49  
50 of larger sizes, so that high magnetic field inhomogeneity is produced, speeding up transverse  
51  
52  
53  
54  
55  
56  
57  
58  
59  
60

1  
2  
3 relaxation of the surrounding water protons due to strong spin dephasing.<sup>3,10-14</sup> Cross-linked  
4 silica or latex matrices have been much praised in the past to encapsulate fluorescent and  
5 magnetic units. Owing to their poor biodegradability capabilities, they are nowadays being  
6 supplanted by hydrophilic polymers and liposomes that simply entrap functional units upon  
7 phase demixing and offer potential clinical transfer.<sup>15-16</sup> However, the later associations face one  
8 main drawback, relying on the absence of specific interactions between the stabilizing  
9 chains/shells and the assembled iron oxide nanoparticles. Uncontrolled progressive release of  
10 SPIONs can occur due to natural liposome rupture or small ion decomplexation, hence steric or  
11 charge repulsions are lost and lead to deleterious nanoparticle agglomeration and reduced  
12 contrast efficiency. Seeking for stable associations with a high magnetic contrast while keeping  
13 hydrodynamic diameters less than 200 nm large thus represent high challenges. Such  
14 nanoassemblies were fabricated in nitric acid, which precluded any further biological use.<sup>17</sup> We  
15 thus resorted to polyelectrolytes such as poly(acrylic acid) (PAA), containing strong iron oxide  
16 chelating units, to stabilize the outer surface of the core-shell structures in water. By contrast,  
17 small citrate ions revealed to be unable to ensure tight cohesion of the whole structure *in vitro*  
18 and conducted to progressive disassembling of the magnetic nanoparticles and fluorescent core.<sup>18</sup>  
19 Thus, PAA has currently appeared as a very attractive biocompatible stabilizing ligand as it  
20 displays strong affinity for iron oxide,<sup>19-20</sup> little toxicity<sup>21</sup> and multiple anchoring points, limiting  
21 its detachment from the iron oxide surface, even after *in vivo* injection.<sup>22</sup> More recently,  
22 poly(phosphonic acid) (PPA) known for its even larger association to iron, was also showed to  
23 form very strong stabilizing shell around SPIONs.<sup>23-24</sup> While most of studies have largely  
24 investigated the impact of the diameter of SPIONs and magnetic nanoassemblies on MRI  
25 contrast and cellular uptake,<sup>5,25</sup> the effects of the polymer shell architecture are much more rarely  
26  
27  
28  
29  
30  
31  
32  
33  
34  
35  
36  
37  
38  
39  
40  
41  
42  
43  
44  
45  
46  
47  
48  
49  
50  
51  
52  
53  
54  
55  
56  
57  
58  
59  
60

1  
2  
3 been scrutinized.<sup>26-27</sup> And yet, evidence has been reported on the consequences of gold  
4 nanoparticle surface structuration (regular versus irregular) with molecular brushes<sup>25,28</sup> onto the  
5 membrane penetration mechanism while polymer geometries (cyclic *versus* linear) of polyester  
6 nanocarriers influence the pharmacokinetics of drug delivery.<sup>29</sup>  
7  
8  
9  
10  
11  
12  
13

14 In order to focus on the impact of the polymer architectures, regardless of the length of  
15 the polymer main chain and the shape of the nanoassemblies (NAs), we have targeted  
16 biocompatible hydrophilic polymers, differing only by their geometry, their hydrophobicity and  
17 chelating strength of SPIONs to stabilize the outer surface of high-density magneto-fluorescent  
18 architectures in water and physiological media. Since pegylation offers limited protein  
19 adsorption and additional increased blood circulation time for further *in vivo* investigations,<sup>8,30</sup>  
20 three distinct architectures containing poly(ethylene glycol) (PEG) chains were explored, varying  
21 in terms of iron oxide chelating affinity (carboxylic *versus* phosphonic acids), hydrophobicity  
22 (with or without alkyl fragment), and compared to PEG-devoid polyelectrolyte.  
23  
24  
25  
26  
27  
28  
29  
30  
31  
32  
33  
34  
35

36 Nuclear magnetic resonance and transmission electron microscopy measurements have  
37 originally been combined with fluorescence ones to investigate the impact of the polymer  
38 coating on the relaxivity properties of the nanoassemblies and gain insight into the structure of  
39 their interface with solutions. To point out the effect of such microstructures on cell interactions,  
40 biological studies, facilitated by the high brightness of the fluorescent nanoassembly platform,  
41 were performed on malignant pleural mesothelioma (MPM) cancer cells, a very severe cancer  
42 contracted after exposure to asbestos and facing poor prognosis of a 12-month median survival  
43 time only with the currently administrated drugs. Fluorescence confocal imaging and MRI  
44 investigations allowed us to track cell uptake of the magneto-fluorescent NAs by two MPM cell  
45 lines and revealed high colloidal and chemical stability, no cytotoxicity effect and progressive  
46  
47  
48  
49  
50  
51  
52  
53  
54  
55  
56  
57  
58  
59  
60

1  
2  
3 internalization over 24 h, the speed of which depends on the polymer nature. These biological  
4  
5 experiments were successfully extended to multicellular tumor cell spheroids (MTCS), known as  
6  
7 dense structures of thousands of self-assembled cancer cells and representing novel responsible  
8  
9 alternative models of solid tumors inoculated in small living animals. All the reported studies  
10  
11 point out the high benefit of using well-controlled polymer coatings such as those issued from  
12  
13 controlled radical polymerization, and provide a very general and simple synthetic approach  
14  
15 towards efficient and versatile multimodal nanolabels for future *in vivo* cell tracking.  
16  
17  
18  
19

## 20 21 **RESULTS AND DISCUSSION**

### 22 23 24 **Fabrication of high-density magneto-fluorescent nanoassemblies**

25  
26 The fabrication of magneto-fluorescent nanoassemblies (NAs) proceeded in two stages that  
27  
28 allowed us to tailor the stabilizing polyelectrolyte without changing the nature and ratio of the  
29  
30 functional constituents of the magneto-fluorescent platform (Figure 1A). In the first step,  
31  
32 SPIONs, fabricated following alkaline coprecipitation of iron(II) and iron(III) salts and further  
33  
34 oxidation of Fe<sub>3</sub>O<sub>4</sub> magnetite into  $\gamma$ -Fe<sub>2</sub>O<sub>3</sub> maghemite with iron(III) nitrate, were dispersed in  
35  
36 nitric acid solutions (pH = 1.4) at a 0.006 wt. % iron concentration.<sup>31</sup> Adding a concentrated  
37  
38 solution of small hydrophobic fluorophores, substituted with phosphonic acid functionality and  
39  
40 endowed with solid-state emission properties, simply formed fluorescent organic nanoparticles  
41  
42 (FONs) upon nanoprecipitation. FONs usually form by adding a water-miscible solution of  
43  
44 fluorophores into a large volume of water. Using water-insoluble fluorophores actually  
45  
46 represents a novel strategy to generate FONs that represent an emerging class of emissive  
47  
48 nanomaterials for sensitive bio-imaging and have proved to induce no cell mortality and low  
49  
50 photobleaching.<sup>32-33</sup> Intermolecular  $\pi$ - $\pi$  aggregation, promoted by hydrophobic effects, causes  
51  
52  
53  
54  
55  
56  
57  
58  
59  
60

spontaneous nanoprecipitation of small hydrophobic fluorophores into bright nanoparticles containing more than  $10^5$  dyes. In our case, the presence of phosphonic units drives self-assembly of SPIONs all around the FON surface through chelation by the outer red-emitting fluorophores placed at the water-FON interface.

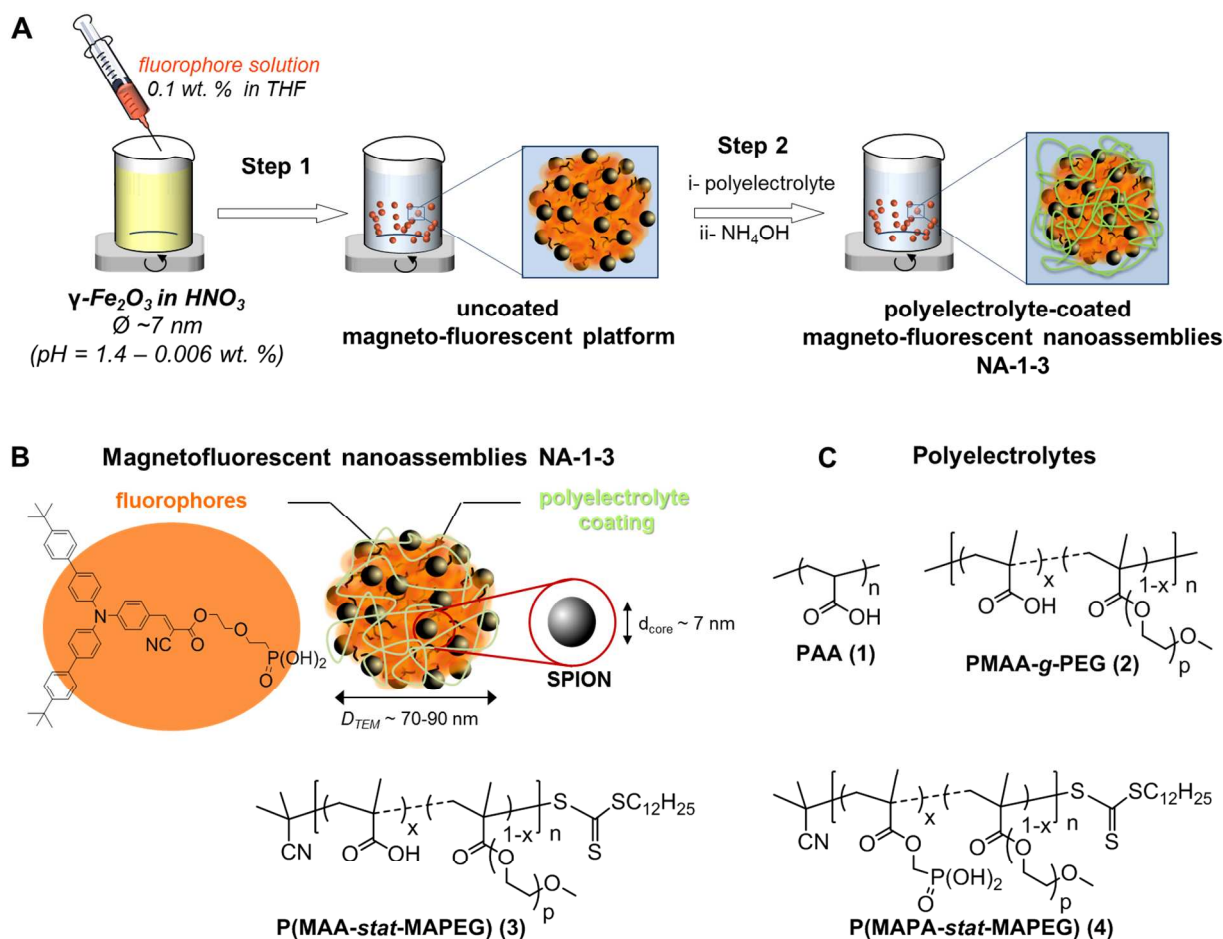


Figure 1. A) Two-step fabrication process of NAs. B) Schematic structure of the magneto-fluorescent NAs stabilized with an anionic polyelectrolyte coating, chelating the shell of magnetic nanoparticles. C) Structure of the synthesized iron oxide-complexing polyelectrolytes.

FON nanoprecipitation actually operates first since SPION complexation requires prior exchange of the labile stabilizing nitrate anions with the strongly interacting phosphonic units.<sup>17</sup>

1  
2  
3 In this way, SPION incorporation inside the organic core does not occur, and raspberry-like  
4  
5 hybrid nanostructures are exclusively obtained with SPIONs attached around the FON surface.  
6  
7

8 The second step of the fabrication process consisted in the colloidal stabilization of the  
9  
10 nanoassembly magnetic shells using polyelectrolytes with strong affinity for iron oxide (Figure  
11  
12 1B). Typical procedure consisting in adding the polyelectrolytes as powders to the acidic  
13  
14 solutions of nanoassemblies, increasing pH to 9 by adding a few drops of 1.3 mol.L<sup>-1</sup> ammonium  
15  
16 hydroxide solution to favor deprotonation of the acidic units. After standing for 15 min, the  
17  
18 solution was dialyzed using membranes with adapted molecular weight cut-off to remove the  
19  
20 non-grafted polymers. To realize such stabilization, various polyelectrolytes with similar sized  
21  
22 main functional chains were targeted and differ in their geometry, charge density and  
23  
24 hydrophobicity. Commercial linear block PAA<sub>2000</sub>-*co*-PEG<sub>2400</sub> copolymers were first used but  
25  
26 revealed unable to generate stable nanoassemblies and only intractable material was obtained.  
27  
28 This effect tends to recall previous studies on 400 nm-large alumina oxide nanoparticles<sup>34</sup>  
29  
30 showing preferential adsorption of block pegylated anionic copolymers involving acrylamido-2-  
31  
32 methylpropanesulfonic acid sodium salt monomers (AMPS-*b*-PEG) over comb-like statistical  
33  
34 copolymers (AMPS-*stat*-PEG). In such block copolymers, the strongly adsorbed sulfonate chains  
35  
36 on the nanoparticle surface led to large aggregates that are however stabilized by electrostatic  
37  
38 repulsions thanks to the long anionic chains (100 units). We suspect here the same phenomenon,  
39  
40 except that the much shorter methacrylate chains (28 units) do not provide enough charge density  
41  
42 to stabilize the nanoassemblies while the PEG chain organization may be partly impaired,  
43  
44 causing inhomogeneous distributions of steric repulsions. We thus privileged comb-like  
45  
46 structures involving poly(methacrylic acid) (PMAA) or poly((methacryloyloxy)-  
47  
48 methylphosphonic acid) (PMAPA) as the main chains, and PEG<sub>2000</sub> or PEG<sub>1100</sub> as the side-chains  
49  
50  
51  
52  
53  
54  
55  
56  
57  
58  
59  
60

1  
2  
3 to allow for a better “crown”-like organization of the polymer, with the (meth)acrylate heads  
4 pointing to the NA and the PEG side-chains extending in water all way around the NA surface.  
5  
6 Short main chains of 25 repetitive units were deliberately targeted since longer chains were  
7  
8 reported to bridge several NAs, causing severe aggregation in water.<sup>18</sup> Hence, four polymers  
9  
10 were used to assess the effects exerted by a controlled polymer topology and composition as well  
11  
12 as the presence of PEG chains on the nanoassembly structures and their interactions with  
13  
14 biological media: commercially available PAA with no PEG units (1), PMAA-*g*-PEG (2) issued  
15  
16 from random esterification of PMAA chains with poly(ethylene glycol), P(MAA-*stat*-MAPEG)  
17  
18 (3), and P(MAPA-*stat*-MAPEG) (4) fabricated following reversible addition-fragmentation chain  
19  
20 transfer (RAFT) polymerization of PEG-vinyl macromonomers with the corresponding  
21  
22 methacrylic acid or (methacryloyloxy)methylphosphonic acid monomers, respectively (Figure  
23  
24 1C). Among the various controlled radical polymerization strategies, RAFT polymerization is  
25  
26 nowadays highly favored since it generates water-soluble and biocompatible polymers with  
27  
28 narrow polydispersity index and finely controlled architectures.<sup>35-36</sup> In addition, it revealed to be  
29  
30 compatible with a large number of functional monomers, and provides easy access to complex  
31  
32 copolymers and ready-to-use terminal reactive groups with no need of protection-deprotection  
33  
34 steps. In this way, polymers containing various chelating units like carboxylate, phosphonate or  
35  
36 sulfur could be easily generated to ensure colloidal stability of metal oxide and metallic  
37  
38 nanoparticles upon efficient complexation.<sup>24,37</sup>

39  
40  
41 The polymer characteristics are gathered in Table 1. The RAFT polymers described in  
42  
43 this contribution bear a trithiocarbonate chain-end. It was previously described that this  
44  
45 functional group does not induce any noticeable cytotoxicity.<sup>38</sup> The 2-cyano-2-propyl dodecyl  
46  
47 trithiocarbonate (CPDTC) functional unit was thus used as a RAFT agent suitable for the  
48  
49  
50  
51  
52  
53  
54  
55  
56  
57  
58  
59  
60

controlled polymerization of methacrylates. Its alkyl substituent advantageously imparts the polymer architecture with additional hydrophobicity, which allowed us to study the direct impact of a partly hydrophobic coating on MRI performance and cellular uptake without modifying the overall number anionic units and their complexing ability.

**Table 1.** Structural characteristics of iron oxide-chelating polyelectrolytes employed as coatings.

Polyelectrolyte	$M_n$ (g.mol <sup>-1</sup> )	$M_w$ (g.mol <sup>-1</sup> )	PI <sup>a</sup>	n <sup>b</sup>	p <sup>b</sup>	x (%) <sup>b</sup>
<b>1</b>	n.a.	$1.8 \times 10^3$	n.a.	24	0	100
<b>2</b>	$5.86 \times 10^4$	$10.9 \times 10^4$	1.87	30	43	78
<b>3</b>	$3.99 \times 10^4$	$5.19 \times 10^4$	1.30	30	43	80
<b>4</b>	$2.68 \times 10^4$	$3.75 \times 10^4$	1.40	25	23	60

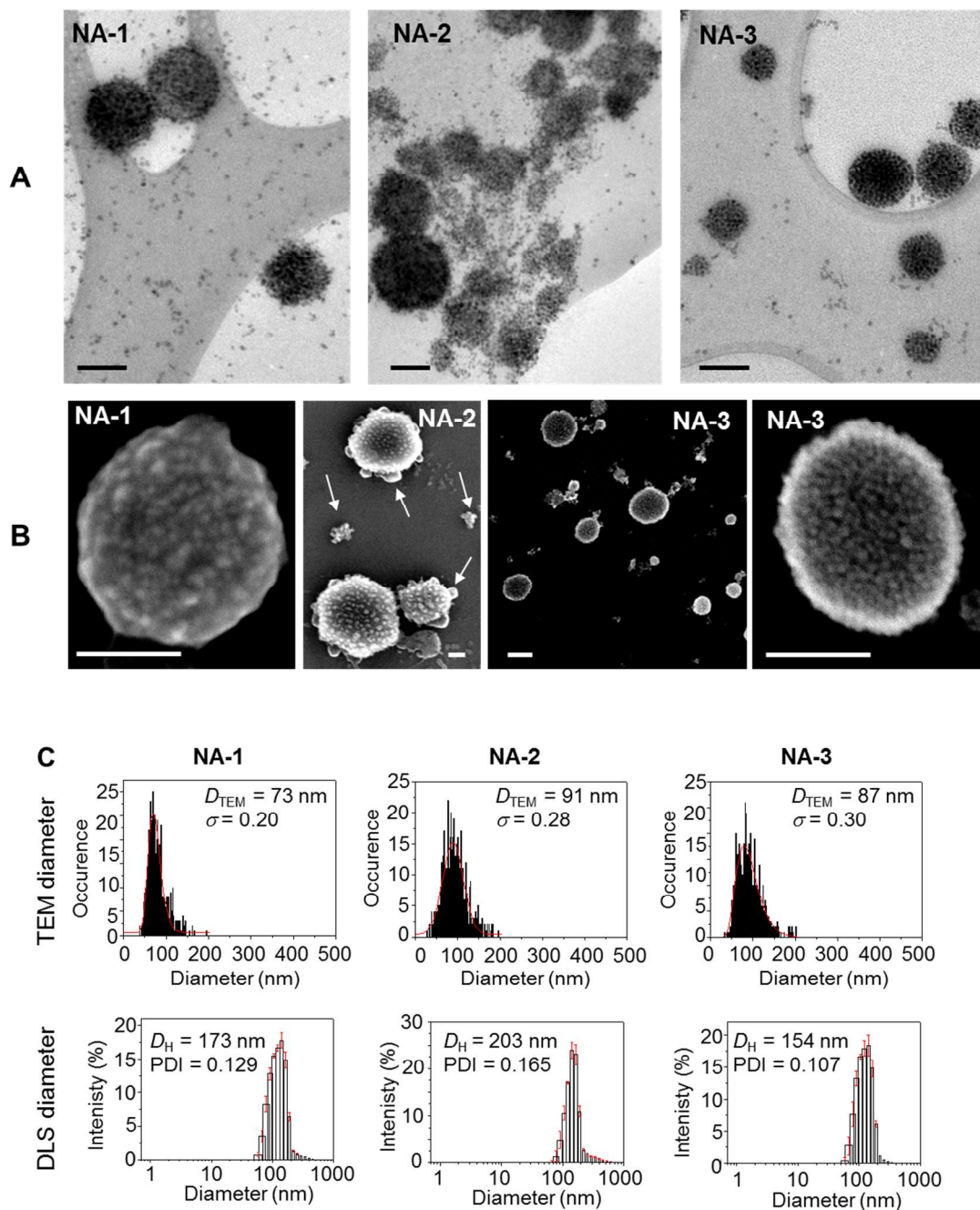
<sup>a</sup> PI designates the polydispersity index determined from size exclusion chromatography analyses using DMF as a solvent. <sup>b</sup> n: degree of polymerization of the main chain; p: degree of polymerization of the side chains; x: molar fraction of the acid comonomer units in the main chain respectively, as depicted in Figure 1C.

The tolerance of the RAFT mechanism to various functional groups enabled the direct copolymerization of a PEG methacrylate macromonomer with either MAA or MAPA, following simple synthetic procedures in solution. The comb-like topology was obtained here by a graft-through method.<sup>39</sup> The statistical distribution of the two types of monomer units was ensured by the similar reactivity ratios of the selected methacrylate comonomers.

### **Influence of the PEG coating and complexing units on the nanoassembly structure**

Transmission electron microscopy (TEM) measurements revealed a tremendous difference in the nanoassembly structure depending on the complexing units of the polyelectrolytes. Phosphonic acid-containing polyelectrolytes yielded neat separation between maghemite nanoparticles and

clearer globules, ascribed to organic matter due to their lower electronic contrast (Figure S1). By contrast, all polyelectrolytes containing carboxylic acid units generated well-defined spherical structures (here dubbed NA-1, NA-2 and NA-3), as showed by TEM imaging (Figures 2A). Here, we want to point out that no such nanoassemblies could be formed by simply mixing polymer solutions with SPIONs (Figure S2).



1  
2  
3 **Figure 2.** A) TEM imaging on holey carbon-coated copper grids, and B) SEM imaging on  
4 silicon wafer of magneto-fluorescent nanoassemblies **NA-1**, **NA-2** and **NA-3**. Scale bar: 100 nm.  
5  
6 White arrows indicate fused or melt nanoassemblies **NA-2**. C) Histograms of diameter  
7 distributions of **NA-1**, **NA-2** and **NA-3** assessed by TEM measurements ( $D_{\text{TEM}}$ ) and DLS  
8 analyses in water ( $D_{\text{H}}$ ). Note that the TEM diameter distributions follow a lognormal function  
9 (red curve).  
10  
11  
12  
13  
14  
15  
16  
17

18 Since TEM imaging of the acidic nanoassembly solution, namely before adding any  
19 polyelectrolyte, showed also the same raspberry-like structure,<sup>17</sup> we concluded that  
20 poly(phosphonic acid) is so complexing with respect to the fluorescent core that it stripped  
21 SPIONs out and pulled them apart. No improvement could be obtained by decreasing the molar  
22 fraction of phosphonic acid monomer units down to 20 % to avoid such competitive  
23 complexation interactions as detected by TEM imaging (Figure S3). Obviously, choosing the  
24 right order in the complexation affinity from the center to the outer part of multi-shell structures  
25 reveals to be crucial to achieve stable NAs and tremendous solubilization of a metal oxide core  
26 upon privileged cation complexation by the shell was even reported in the past.<sup>40</sup> A similar  
27 situation was already observed when the fluorophores of the core were substituted with a  
28 carboxylic acid unit.<sup>18</sup> The latter proved insufficient to retain the complexed iron oxide  
29 nanoparticles after coating with poly(acrylic acid) exerting competitive multifold attachment.  
30 Hence, only PAA (**1**) and PMAA-based polyelectrolytes (**2**) and (**3**) were retained for the  
31 following studies.  
32  
33  
34  
35  
36  
37  
38  
39  
40  
41  
42  
43  
44  
45  
46  
47  
48  
49  
50

51  
52 When looking carefully at the corresponding NA structure as a function of the polyelectrolyte  
53 structure, a superior density of SPIONs could be observed at the surface of both **NA-2** and **NA-3**.  
54 For the latter two, less isolated maghemite nanoparticles could be observed contrary to **NA-1**  
55  
56  
57  
58  
59  
60

1  
2  
3 involving a PAA stabilizing coating (Figure 2A). Interestingly, scanning electron microscopy  
4 (SEM) imaging reveals nanoassemblies twice as large as those detected by TEM, along with  
5  
6 giant well-defined aggregates (400-500 nm-large) (Figure 2B). Since argon plasma treatment for  
7  
8 a few seconds was applied to gain electronic contrast, we suspect partial melting of the self-  
9  
10 assembled organic core of the nanoassemblies and even fusion for several of them. This results in  
11  
12 enlarged diameters as well as large aggregates with small peripheral protuberances (especially  
13  
14 for **NA-2**) ascribed to the initial nanoassemblies. Thus, SEM imaging indirectly indicated the  
15  
16 soft core's character of the raspberry-like magneto-fluorescent nanoassemblies. Overall, the  
17  
18 mean dry diameters  $D_{\text{TEM}}$  evaluated by TEM size lognormal distribution varied between 70 and  
19  
20 90 nm with a relatively low standard deviation ( $\sigma < 0.30$ ) (Table 2-Figure 2C). The pegylated  
21  
22 NAs were found slightly larger by a few nm as a result of the larger size of polymers **(2)** and **(3)**.  
23  
24 Interestingly, the hydrodynamic diameters  $D_{\text{H}}$  of NA dispersions in water, measured by dynamic  
25  
26 light scattering (DLS), followed quite a distinct trend. The  $D_{\text{H}}$  values were found at 170-200 nm,  
27  
28 systematically larger than the dry diameter  $D_{\text{TEM}}$  ones, as a result of the surrounding hydration  
29  
30 shells. The nanoassemblies **NA-3** appeared smaller with  $D_{\text{H}} = 154$  nm, which suggests a less  
31  
32 extended coating in water due to the presence of the hydrophobic<sup>41</sup> chains of the RAFT agent, as  
33  
34 already reported for PEG chains grafted to phospholipids with long alkyl chains.<sup>42</sup> The lack of  
35  
36 similar trends between both  $D_{\text{H}}$  and  $D_{\text{TEM}}$  values emphasizes the importance of complementary  
37  
38 measurements and the complex impact of coulombic and dipolar interactions on the recruitment  
39  
40 of water molecules, as also exemplified by the charge potential  $\zeta$  measurements. A lesser zeta  
41  
42 potential  $\zeta$  was found for **NA-2** with PMAA-g-PEG coating, issued from conventional  
43  
44 polymerization whereas **NA-1** and **NA-3** with PAA and RAFT-based coatings respectively,  
45  
46 yielded largely negative  $\zeta$  values ( $\zeta < -51$  mV). All nanoassemblies show similar hydrodynamic  
47  
48  
49  
50  
51  
52  
53  
54  
55  
56  
57  
58  
59  
60

diameters in water, NaCl solutions of varying concentration (0.1, 0.3 and 0.5 mmol.L<sup>-1</sup>), HBSS and RPMI, indicating no aggregation process (Figure S4A). A 15-day follow-up of the nanoassemblies in potential storage media (water, NaCl, HBSS) revealed also large colloidal stability since no aggregation could be detected (Figure S4B). Far from being contradictory, the large absolute  $\zeta$  value and the low  $D_H$  value for **NA-3** indicate the formation of a very compact shell of PEG chains at the nanoassembly surface, leaving few access to water molecules, which can exert quite an influence on the MRI contrast and relaxivity properties.

**Table 2.** Structural and photophysical characterizations of magneto-fluorescent NAs coated with PAA (**1**), PMAA-*g*-PEG (**2**) and P(MAA-*stat*-MAPEG) (**3**) polyelectrolytes.

NA	$D_{TEM}$ (nm) (Std Deviation)	$D_H$ (nm) / PDI	$\zeta$ (mV)	[Fe] (mM)	$\lambda^{max}(\text{abs})$ (nm)	$\lambda^{max}(\text{em})$ (nm)	$\Phi_f$ ( $\times 10^{-2}$ )
<b>NA-1</b>	73 (0.20)	173 / 0.129	$-51.9 \pm 6.4$	0.384	423	614	1.45
<b>NA-2</b>	91 (0.28)	203 / 0.165	$-32.6 \pm 5.7$	0.543	428	612	0.83
<b>NA-3</b>	87 (0.30)	154 / 0.107	$-53.0 \pm 10.5$	0.459	429	595	0.20

### Photophysical properties and impact of the polymer coating on emission properties

The absorption spectra of NAs appear very similar and the contributions of the three structural components could be noticed (Figure 3): i-the low-energy band at 420 nm is ascribed to a charge transfer transition within the FONs' fluorophores; ii-the monotonous increase in absorbance at higher energy relies on the  $\gamma$ -Fe<sub>2</sub>O<sub>3</sub> nanoparticle extinction spectrum; iii- finally, the large tail around 200-250 nm is related to the UV absorption of the C=O chromophores contained in the PAA or PMMA carboxylate units (Figure S5). For P(MAA-*stat*-MAPEG) coating, one could

distinguish an additional maximum at 311 nm that is characteristic of the RAFT trithiocarbonate ends, remaining uncleaved after treatment with ammonia.<sup>43</sup> Excitation in the absorption band of the fluorophores at 450 nm provided an emission signal whose maximum varies between 595 and 614 nm (Figure 3, Table 2). This emission band is typical of the FON core one which is centered at 605 nm in water in the absence of SPIONs.<sup>44</sup> The large Stokes shift, defined as the difference in energy between the absorption and emission maxima of the nanoassembly spectra, were found around 7000  $\text{cm}^{-1}$ . This large energy difference is worth noting since it greatly facilitates label detection in live cells where endogenous fluorophores usually display autofluorescence, weakly shifted from excitation.

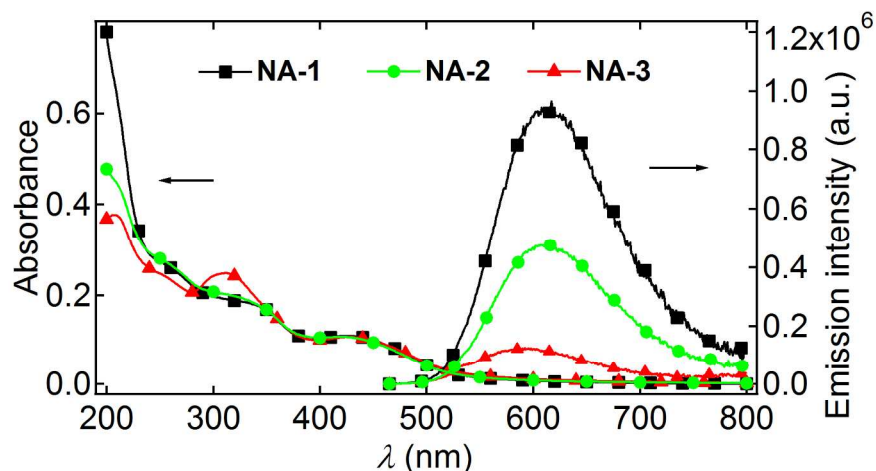


**Figure 3.** UV-vis absorption (left axis) and emission (right axis,  $\lambda_{exc} = 450$  nm) of aqueous solutions of magneto-fluorescent nanoassemblies NA-1, NA-2 and NA-3.

Since the FON fluorophores display strong positive solvatochromism,<sup>45-46</sup> the hypsochromic shift observed for NA-3 compared to NA-1 and NA-2 again reflects significant differences in the interactions with water molecules, which may stem from the lipophilic chains of the RAFT-ends organized in a close and tight fashion at the surface of the magneto-

1  
2  
3 fluorescent structures. Such assumption is reinforced by the notable decrease in fluorescence  
4 emission quantum yield observed with **NA-3** compared to the other two NAs. Recent studies  
5 have actually reported on the efficient dynamic and static emission quenching of fluorophores in  
6 the presence of RAFT polymers containing dithiocarbonate transfer agents,<sup>47</sup> which implies close  
7 vicinity between RAFT polymers and fluorophores. Such dynamic quenching was also  
8 confirmed by fluorescence time-resolved measurements recorded at 600 nm after a 450 nm  
9 excitation (Table S1-Figure S6). A four exponential fit was required to model the fluorescence  
10 decay. While the major three lifetime components  $\tau_2$ ,  $\tau_3$  and  $\tau_4$  were found almost identical for  
11 all nanoassemblies at 0.52-0.57, 0.14-0.16 and 0.02-0.03 ns respectively, the longer component  
12  $\tau_1$  largely differs between **NA-3** at 1.07 ns, and **NA-1** and **NA-2** at around 2 ns. From the  
13 intensity-averaged fractions, the latter time component contributes to the total emission decay by  
14 only 1.5-5 %. We thus presume that  $\tau_1$  characterizes the fluorophores that are placed at the  
15 periphery of the nanoplatform and sense in a more privileged way the polyelectrolyte coating.  
16 The quenching phenomenon observed for **NA-3** thus indirectly proves the strong attachment of  
17 RAFT-derived P(MAA-*stat*-MAPEG) at the surface of the magneto-fluorescent nanoassemblies  
18 since dynamic quenching is very negligible at concentrations as low as  $10^{-4}$  mol.L<sup>-1</sup> for both the  
19 polyelectrolyte and fluorescent units.

20  
21 All the above-reported structural and photophysical characterizations conduct us to  
22 propose a tentative scheme to describe the organization and extension of the polyelectrolyte  
23 chains around the FON surface, which would lead for polyelectrolyte (**3**) to stronger interchain  
24 interactions with  $\gamma$ -Fe<sub>2</sub>O<sub>3</sub> nanoparticles due to the less extended chains, especially in water  
25 (Figure S7).  
26  
27  
28  
29  
30  
31  
32  
33  
34  
35  
36  
37  
38  
39  
40  
41  
42  
43  
44  
45  
46  
47  
48  
49  
50  
51  
52  
53  
54  
55  
56  
57  
58  
59  
60

## ZFC-FC magnetic measurements and low-temperature hysteresis

In order to probe the possible influence of the polyelectrolyte coating onto the magnetic properties of the nanoassemblies, we performed static magnetic measurements. Zero-field-cooled (ZFC) and field-cooled (FC) curves, giving information on magnetic interactions between SPIONs at the FON surface, were traced by recording the temperature dependence of the magnetization under a 50 Oe magnetic field (Figure 4A).

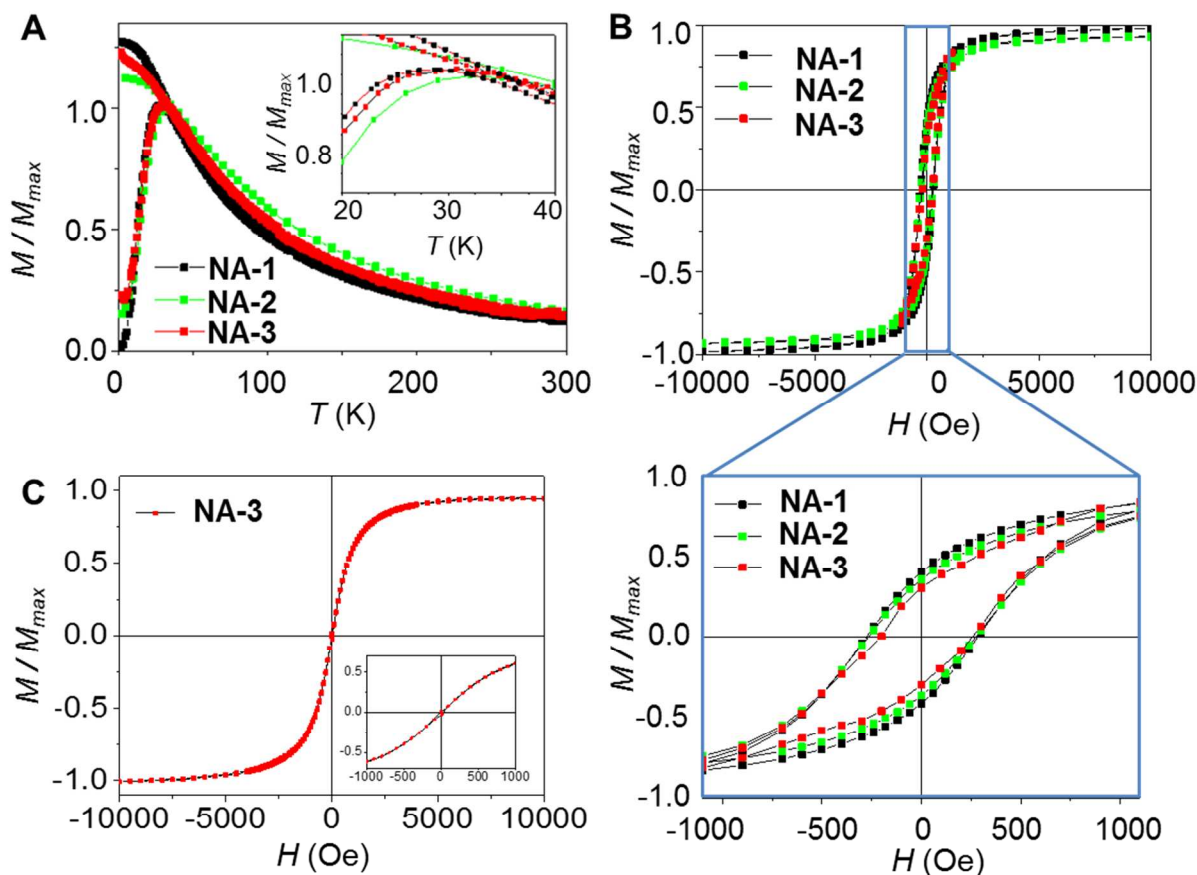


**Figure 4.** A) ZFC-FC curves for magneto-fluorescent nanoassemblies NA-1, NA-2 and NA-3; the curves are normalized to the maximum of the ZFC magnetizations. B) Plot of magnetization  $M/M_{max}$  versus applied magnetic field at 2.5 K and enlargement at low magnetic fields. C) Plot of magnetization  $M/M_{max}$  versus applied magnetic field at 310 K for nanoassemblies NA-3.

1  
2  
3 For all samples, the thermal irreversibility characteristic of an assembly of single domain  
4 magnetic particles is observed below ca. 40 K, pointing out that the investigated systems are in  
5 the superparamagnetic state at room temperature. Except for a slight shift of the maximal  
6 temperature  $T_{\max}$  at 35 and 33 K for NA-2 and NA-3 respectively, against 28 K for NA-1 signing  
7 larger dipole-dipole interactions and more closely arranged SPIONs upon coating with pegylated  
8 polyelectrolytes (Table 3), all curves display the same shape in agreement with the same general  
9 NA architecture and identical sized SPIONs (Figure 4A). We thus recorded the magnetization  
10 evolution as a function of the magnetic field at 2.5 K where ZFC-FC measurements indicate that  
11 SPIONs are blocked in their ferromagnetic state (Figure 4B). Again, the magnetization curves  
12 superimposed fairly well with the values of the reduced remanence  $M_R/M_S$  (namely, the ratio of  
13 the remanence to saturation magnetization) in the 0.32-0.40 range, which as commonly observed  
14 for maghemite nanoparticles.<sup>15</sup> Similarly, the coercive field  $H_c$  for all samples also changed only  
15 slightly from 18 to 22 kA.m<sup>-1</sup> (226 to 276 Oe) when varying the nature of the polyelectrolyte  
16 coating. Conversely, at room temperature, namely 310 K, no irreversibility was observed,  
17 indicating that all nanoassemblies are in the superparamagnetic state (Figure 4C and Figure S8).

18  
19  
20 From these measurements, we can thus conclude that the static magnetic properties of all NAs  
21 are exclusively ruled by the shell of SPIONs attached on the FON core, and are almost  
22 independent of the nature of the polyelectrolyte coating.

### 23 **NMRD measurements and MRI contrast as a function of the polyelectrolyte coating**

24  
25 As MRI contrast brought by SPIONs is dictated by their relaxivity properties, we recorded their  
26 NMRD profiles which give access to the longitudinal  $r_1$  and transverse  $r_2$  relaxivities. Since  
27 relaxation of water protons close to the NA surface is also probed, any microscopic difference  
28 due to the polyelectrolyte coating can be inferred (Figure 5). The difference between the data  
29  
30  
31  
32  
33  
34  
35  
36  
37  
38  
39  
40  
41  
42  
43  
44  
45  
46  
47  
48  
49  
50  
51  
52  
53  
54  
55  
56  
57  
58  
59  
60

recorded at room and physiological temperatures being within 10 %, we reported the NMR results obtained at room temperature to better discuss the physical mechanisms involved in the nuclear relaxation. For comparison purposes with a clinically used contrast agent, we retained Endorem® made of a multicore structure ( $D_H \sim 120$  nm) of 5 nm-large SPIONs self-assembled with dextran polymer.

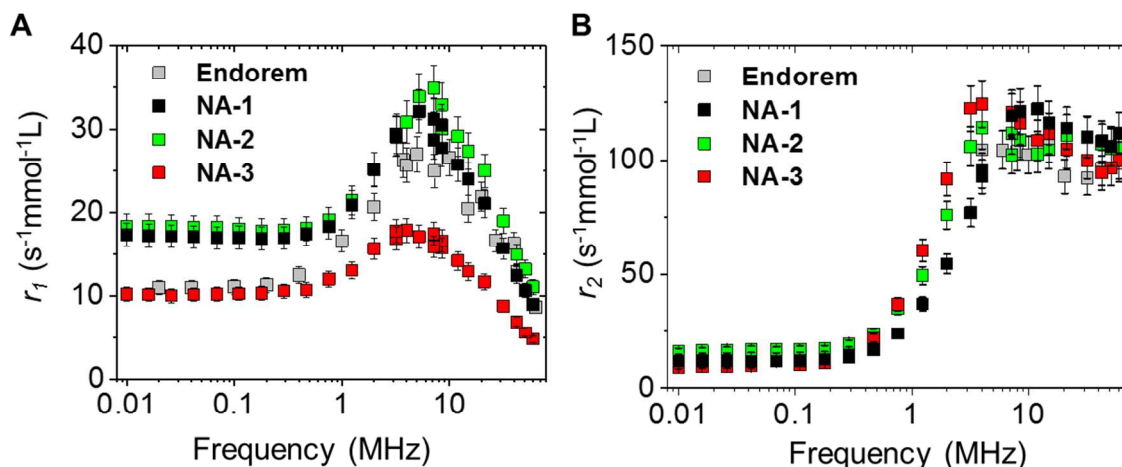


**Figure 5.** A) Longitudinal  $r_1$ , and B) transverse  $r_2$  relaxivities of nanoassemblies NA-1, NA-2, NA-3 and commercial contrast agent Endorem® as a function of proton Larmor frequency.

As SPIONs induce strong distortions of the local magnetic field, proton relaxation is largely dominated by a spin-spin relaxation mechanism, giving rise to  $r_2$  relaxivities by far larger than  $r_1$  ones for frequencies higher than several MHz. Hence, most of the studies have focused on measuring  $r_2$  values just at the (very few) clinical fields,<sup>12-13,48-49</sup> but do not report on  $r_1$  vs frequency behavior. And yet, the later investigations provide precious information on the dominant mechanisms of nuclear relaxation in different frequency ranges and on the water diffusion time. Therefore, they give insight into the nanoassembly structure, its spin dynamics and the hydrated environment. The  $r_1$  vs frequency ( $\nu$ ) profiles for all three NAs display a typical superparamagnetic behavior: a decrease in relaxivity at high frequency, a mid-field peak at  $\nu_{\max}$ ,

and a low field plateau (Figure 5A).<sup>50</sup> Interestingly, the typical “dispersion” feature for SPIONs with diameter less than 10 nm, occurring between the frequency corresponding to the maximum  $r_l$  and the low frequency region, does not appear clearly in the  $r_l(\nu)$  curves. Since the dispersion, generally reduced for small particles, is correlated to the magnetic anisotropy of the SPIONs, we can conclude in the case of NAs on an increase in anisotropy.<sup>51</sup> At high frequencies, Curie relaxation prevails due to the presence of a high local magnetic field induced by the magnetization of SPIONs, subjected to a relatively high external static magnetic field, this local field being dynamically mediated by the diffusion correlation time. The curves for all NAs converge toward similar values as expected for the studied samples, displaying identical static magnetic behaviors. The most striking features are the significantly lower  $r_l$  values found for **NA-3** at  $\nu_{max}$  and in the low frequency region (Table 3).

**Table 3.** Maximum longitudinal  $r_l$  and transverse  $r_2$  relaxivities [@corresponding frequency], and  $r_2/r_l$  ratio measured at 25 °C for nanoassemblies **NA-1**, **NA-2** and **NA-3**, and commercial contrast agent Endorem® for comparison, and magnetic properties of nanoassemblies **NA-1**, **NA-2** and **NA-3** measured at 2.5 K.

	$r_{lmax}$ (s <sup>-1</sup> mmol <sup>-1</sup> L) [@ $\nu$ (MHz)]	$r_{2max}$ (s <sup>-1</sup> mmol <sup>-1</sup> L) [@ $\nu$ (MHz)]	$r_2/r_l$ @8.5 / 21.3 / 60 MHz	$T_{max}$ (K)	$H_c$ (kAm <sup>-1</sup> )	$M_r/M_s$
<b>NA-1</b>	32 [6]	122 [12]	4 / 5 / 12	28	22	0.40
<b>NA-2</b>	34 [7]	115 [4]	3 / 4 / 9	35	22	0.35
<b>NA-3</b>	19 [5]	125 [4]	7 / 9 / 21	33	18	0.32
<b>Endorem®</b>	28 [7]	105 [4]	4 / 5 / 11	-	-	-

Since all NAs share the same core-shell configuration and static magnetic properties, the difference encountered in the  $r_l$  relaxivity of **NA-3** cannot be related to the latter effects. We

1  
2  
3 suggest a possible explanation that could rely on the dynamics of water molecules, namely their  
4 diffusion, retention time as well as their access closer or farther from to the magnetic shell.<sup>42,52</sup>  
5  
6 The smaller hydration sphere found for **NA-3** by DLS (see Table 2) suggests the existence of a  
7  
8 restricted solvation sphere due to strongly attached PEG side-chains and hydrophobic dodecyl  
9  
10 RAFT-end chains. At a first glance, the restricted solvation sphere could erroneously evoke a  
11  
12 closer diffusion of water to the NA surface. Actually, the presence of a hydrophobic part in the  
13  
14 **NA-3** polyelectrolyte prevents water to diffuse into the coating, while the hydrophilicity of the  
15  
16 other nano-assemblies allows water molecules to move closer to the SPIONs core inside the NA  
17  
18 coating itself. Therefore the difference in  $r_1$  relaxivity could be explained by the presence of  
19  
20 dodecyl RAFT-end chains in **NA-3**.  
21  
22  
23  
24  
25  
26  
27

28 Contrarily to  $r_1$  dispersions, similar  $r_2$  profiles were found for all NAs with maximum  $r_2$  values  
29  
30 of around  $120 \text{ s}^{-1}\text{mmol}^{-1}\text{L}$  in agreement with identical magnetic cores (Figure 5B). In fact, local  
31  
32 dephasing of the nuclear magnetization is mostly caused by the high electronic magnetization of  
33  
34 the SPIONs clustered around the FON core. This represents the prevailing mechanism inducing  
35  
36 nuclear transverse relaxation, which is partially described by an approximate heuristic model in the  
37  
38 framework of the so called Motional Average Regime (MAR).<sup>10,53</sup> Unfortunately, the actual models (like  
39  
40 the universal scaling law proposed by Sandre et al.)<sup>54</sup> are not able to describe the whole transverse NMRD  
41  
42 curve ( $r_2$  vs.  $\nu$ ) or explain the relaxation mechanisms as a function of the applied magnetic field.  
43  
44 Nevertheless, since the transverse relaxivity  $r_2$  represents the fundamental parameter to assess the MRI  
45  
46 efficiency for a superparamagnetic material, the reported experimental data demonstrate that our  
47  
48 nanoparticles act as promising negative contrast agents. Moreover, the low  $r_1$  and high  $r_2$  values for  
49  
50 **NA-3** yields a large  $r_2/r_1$  ratio that represents a parameter as important as  $r_2$  relaxivity to assess  
51  
52 the efficiency of negative contrast agents. In the case of **NA-3**, such ratio is about 21 at 60 MHz  
53  
54  
55  
56  
57  
58  
59  
60

1  
2  
3 clinical frequency, which is two to threefold higher than those for **NA-1**, **NA-2** and Endorem®.  
4  
5 These NMRD studies demonstrate the large importance of considering both the transverse and  
6  
7 longitudinal relaxivities to probe the interface of complex magnetic nanostructures and evaluate  
8  
9 the microscopic mechanisms underlying the nuclear relaxation that is quite largely influenced by  
10  
11 the spin topology and water diffusion path. Deciphering the fundamental physical mechanisms  
12  
13 ruling the nuclear relaxation should thus open novel perspectives regarding the synthesis of  
14  
15 novel coatings with high efficiency (namely, higher transverse and/or longitudinal relaxivities)  
16  
17 for improved MRI contrast.  
18  
19  
20  
21

### 22 23 **Kinetics of cellular internalization and cell toxicity assays in mesothelioma cancer cells**

24  
25 Adherent mesothelioma cells (Meso 11), a cell line established from pleural fluid of patients  
26  
27 affected by MPM, were incubated with **NA-1**, **NA-2** and **NA-3** in RPMI medium supplemented  
28  
29 with 10 % serum. The amount of administrated nanoassemblies was referred to their iron  
30  
31 content, titrated by elemental analyses by means of inductively coupled plasma optical emission  
32  
33 spectrometry (ICP-OES) following acidic mineralization. Kinetics of NAs' uptake was carried  
34  
35 out by following the fluorescence and magnetic responses of single cells. The fluorescent signal  
36  
37 and cell viability were assessed by means of imaging flow cytometry after usual protocols to  
38  
39 detach the cells, and treatment for 30 min with Zombie NIR®, serving as a fluorescent marker  
40  
41 that lights up in the presence of dead cells. In this way, a single excitation at 488 nm allowed for  
42  
43 dual excitation of the nanoassemblies and fluorescent marker, and simultaneous detection of  
44  
45 their respective emission signals in two distinct non-overlapping channels (channel 3: 560-595  
46  
47 nm for NAs; channel 12: 745-800 nm for Zombie NIR® permeant to dead cells). Figure 6A  
48  
49 displays the kinetics of uptake over a 24 h incubation period for **NA-1**, **NA-2** and **NA-3**, at an  
50  
51  
52  
53  
54  
55  
56  
57  
58  
59  
60

iron concentration of  $2\text{-}3\ \mu\text{mol.L}^{-1}$ . The mean fluorescence intensity (MFI) steadily increased for all three nanoassemblies and started saturating after around 16 h for NA-1 and NA-2.

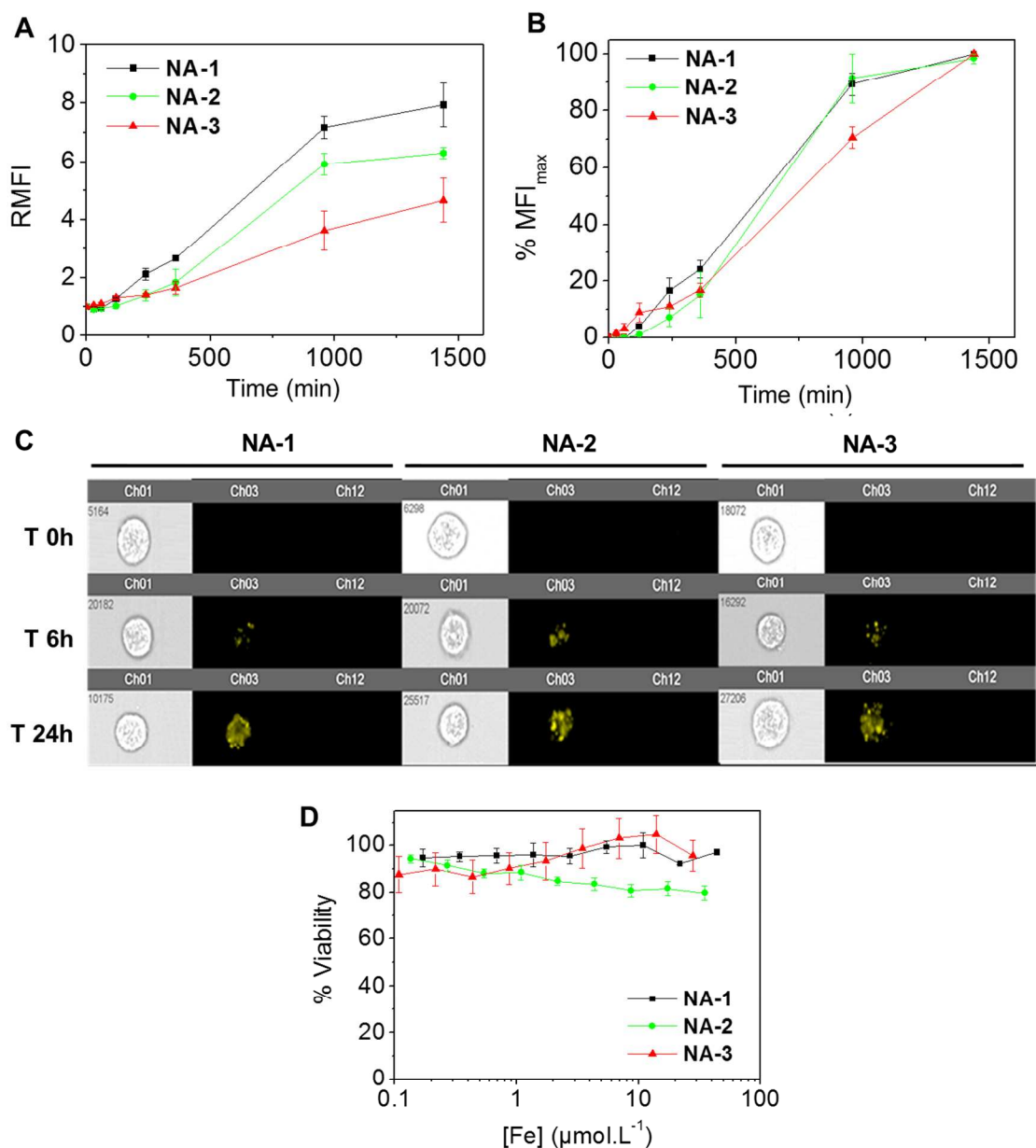


**Figure 6.** Meso 11 cells incubated with nanoassemblies NA-1, NA-2 and NA-3 in RPMI supplemented with 10 % FBS serum. A) Absolute, and B) normalized mean fluorescence intensity (MFI) evolution over time of incubation. C) Imaging flow cytometry at 0 h, 6 h and 24 h. D) Cell viability assay after a 72 h incubation period for  $[\text{Fe}] = 0.1\text{-}100\ \mu\text{mol.L}^{-1}$ .

1  
2  
3 At very early times up to 4 h, only a few nanoassemblies were internalized. This result  
4 was confirmed by imaging flow cytometry showing dimmed fluorescence signals at 6 h and very  
5 bright ones at 24 h inside the cells (Figure 6C). The slow rate of uptake is actually related to the  
6 negative charge of the investigated nanoassemblies that have to overcome the electrostatic  
7 repulsions exerted by the phospholipids of the cytoplasmic membrane.<sup>55</sup> Interestingly, at longer  
8 times, **NA-3** tend to internalize at a significantly slower rate compared to **NA-1** and **NA-2**, as  
9 exemplified by the normalized MFI signal (Figure 6B). This result is quite surprising since both  
10 PMAA-g-PEG and P(MAA-*stat*-MAPEG) contain the same functional groups and PEG chain  
11 length. At first, one could think at differential interactions with the serum proteins that adsorb on  
12 the nanoparticle surface and govern the dynamic of uptake.  
13  
14  
15  
16  
17  
18  
19  
20  
21  
22  
23  
24  
25  
26

27 We thus investigated by electrophoresis the nature of the protein corona that could form  
28 around all three kinds of nanoassemblies. The latter were incubated for 1 h at an iron  
29 concentration of  $[\text{Fe}] = 2.1 - 2.9 \text{ mmol.L}^{-1}$  in cell culture medium (RPMI medium supplemented  
30 with 10 % FBS). The nanoparticle-protein complexes were extracted by centrifugation and the  
31 supernatant loaded into the wells of a polyacrylamide electrophoresis gel. After migration for 90  
32 min and revelation under UV irradiation, three bands for all NAs were visible (Figure S9). One  
33 of them was found in the range of 50-60 kDa molecular weight and could be identified as being  
34 bovine serum albumin (BSA), as confirmed by comparative elution of a BSA reference sample.  
35 The other two bands were found in the range of 10-30 kDa and attributed to apolipoproteins  
36 (apoAI and apoAII) in agreement with common reports in the literature regarding the  
37 interactions of iron oxide nanoparticles with human serum proteins.<sup>56-57</sup> It is worth noting that  
38 very few non-specific interactions occur between the nanoassemblies and cell culture medium  
39 despite the relatively high NA concentration used in the study to distinguish protein complex  
40  
41  
42  
43  
44  
45  
46  
47  
48  
49  
50  
51  
52  
53  
54  
55  
56  
57  
58  
59  
60

1  
2  
3 traces. This observation features weak protein adsorption, which is highly sought for further *in*  
4  
5 *vivo* investigations. As all three NAs display the same patterns under the investigated  
6  
7 experimental conditions, we can reasonably ascribe the distinct uptake rates of **NA-3**  
8  
9 nanoassemblies to their intrinsic comb-like polyelectrolyte coating. As deduced from the above  
10  
11 photophysical and magnetic studies, the hydrophobic RAFT polymers tend to organize in quite a  
12  
13 compact fashion at the nanoassembly surface. The generated nanoarchitectures thus display a  
14  
15 distinctly structured surface, which makes the uptake rate continuous with no negative impact on  
16  
17 cell viability.  
18  
19  
20

21  
22 This observation is of utmost importance as the actual tendency is to advertise fast uptake  
23  
24 for fast therapeutics delivery with little consideration of cytotoxicity. Indeed, positively charged  
25  
26 nano-objects display faster internalization in usually less than 1 h, which causes large cell  
27  
28 mortality due to extensive permeation of the cell membrane, unable to readapt in front of the  
29  
30 sudden flow of nanoparticles.<sup>58</sup> In our case, cell viability assay based on the use of 3-[4,5-  
31  
32 dimethylthiazol-2-yl]-2,5- diphenyltetrazolium bromide compound (MTT reagent) after 72 h of  
33  
34 incubation with the different NAs, revealed no cytotoxicity for **NA-3** and **NA-1** over the broad  
35  
36 range of iron concentrations from 0.1 to 100  $\mu\text{mol.L}^{-1}$  (Figure 6D). A slightly higher level of  
37  
38 cytotoxicity for **NA-2** was found although such a value, below 20 %, is often regarded as non-  
39  
40 significant. The images collected using imaging flow cytometry show no change in the cell  
41  
42 phenotype over 24 h, which reinforces the non-cytotoxic properties of all nanoassemblies (Figure  
43  
44 6C). To ascertain the cellular entry of both the magnetic and fluorescent components of the  
45  
46 nanoassemblies, complementary magnetophoresis measurements were performed on cells  
47  
48 incubated with Meso 11 after 4 h, 8 h and 24 h ( $[\text{Fe}]=200 \mu\text{mol}^{-1}$ ). Such experiments consist in  
49  
50 measuring the velocity of cells subjected to a magnetic field gradient, which is directly correlated  
51  
52  
53  
54  
55  
56  
57  
58  
59  
60

1  
2  
3 with the cellular load of iron oxide. Due to the low amount of magnetic materials used with  
4 regard to literature and the associated uncertainty, comparative results between the distinctly  
5 coated NAs would be irrelevant. As illustrated in Figure S10, all NAs nicely followed the same  
6 trend of continuous iron oxide uptake over 24 h. These results indicate tight association of both  
7 the magnetic shell onto the fluorescent core, making such nano-objects particularly attractive for  
8 bimodal imaging. They thus emphasize the clear advantage of nanoassemblies comprising FONs  
9 as fluorescent cores and a shell of magnetic nanoparticles. In this way, very bright fluorescent  
10 and magnetic nanostructures are obtained, enabling high detection sensitivity and easy follow-  
11 up.  
12  
13  
14  
15  
16  
17  
18  
19  
20  
21  
22  
23  
24

### 25 **Multimodal imaging properties in live cells**

26  
27  
28 To prove the potentiality of the magneto-fluorescent NAs as multimodal imaging agents, we  
29 performed confocal fluorescence microscopy, MRI and TEM investigations of cells after NA  
30 incubation for 24 h. The culture medium was washed with PBS to remove NAs in excess. The  
31 cells were treated successively with Alexa Fluor® 647 conjugate of wheat germ agglutinin  
32 (WGA) (green) and Hoechst (blue) to stain the cell membranes and nuclei respectively (Figure  
33 7A). Confocal fluorescence imaging revealed very bright dots, depicted in red, which can be  
34 assigned to internalized NAs. An XY projection clearly revealed the internalization of NA and  
35 their unambiguous location inside the cytoplasm. Again, no impact of the nanoassemblies could  
36 be noticed on the adherent Meso 11 cells that keep their elongated shape, which confirms the cell  
37 viability assays and absence of cytotoxicity. To gain even better definition of the NA location,  
38 we took advantage of the iron oxide electronic contrast and performed TEM experiments. Most  
39 of protocols involve cell detachment and centrifugation to generate a cell pellet, which can  
40 damage the cell architecture. To avoid partial cell destructuration, cells were directly fixed in  
41  
42  
43  
44  
45  
46  
47  
48  
49  
50  
51  
52  
53  
54  
55  
56  
57  
58  
59  
60

Epon resin and properly stained. TEM observation of the cell monolayers showed well-contrasted dark dots, included in larger structures that remind of endosomes, especially for NA-1 (Figure 7B).

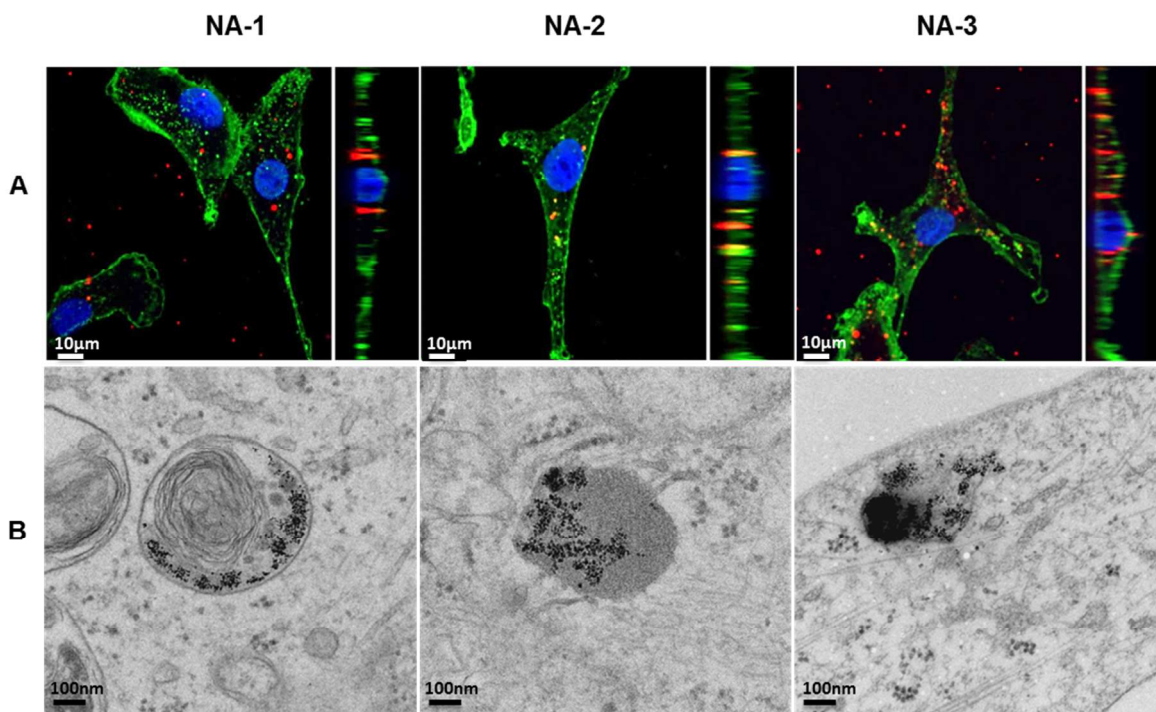


**Figure 7.** Meso 11 cells incubated with magneto-fluorescent nanoassemblies NA-1, NA-2 and NA-3 for 24 h. A) Confocal fluorescence microscopy showing the nanoassemblies in red, the WGA-AlexaFluor® 647-stained cellular membrane in green, and the Hoechst-stained nuclei in blue. Pictures include an XY orthogonal projection. B) TEM imaging of fixed cells.

Careful observations at such a magnification let us notice small packets of dark dots instead of a random dispersion. This feature is to correlate with previous *in vivo* and *in vitro* observations where the magneto-fluorescent structure was kept, with no dissembling of the fluorescent core from the magnetic shell.<sup>22</sup> Therefore, incrementing stabilizing PMAA or PAA-based polyelectrolyte coating with PEG chains does not impair the emission properties and the

1  
2  
3 ability of generating tight hybrid nanoassemblies. The novel pegylated NAs thus represent very  
4 attractive agents for correlative light electron microscopy that is currently stirring much attention  
5 since high spatial resolution of biological structures can henceforth be achieved.<sup>2</sup>  
6  
7  
8  
9

10 The NA multimodality property is extended to MRI investigations to anticipate *in vivo*  
11 experiments in the future. A novel series of cells incubated with the magneto-fluorescent NAs at  
12 an iron concentration of 2-3  $\mu\text{mol.L}^{-1}$  for 24 h was prepared. It is worth noting that such a  
13 concentration is actually 10 to  $10^2$  times lower than the commonly recommended iron doses for  
14 conventional MRI on humans (0.5-10  $\text{mg.kg}^{-1}$ ).<sup>5960</sup> After the usual recuperation procedure, the  
15 cells were deposited in small wells dug into a matrix of well-degassed 1 % low-melting agarose  
16 gel, filling a glass cylinder (Figure 8A).<sup>61</sup> The wells were sealed by pouring on top a still-liquid  
17 and cooled agarose solution. Careful air degassing is requested to avoid dramatic quenching  
18 effects of MRI contrast due to entrapped paramagnetic dioxygen. A T2 sequence was used in  
19 relation with the negative contrast properties of iron oxide nanoparticles. Unlike control cells  
20 devoid of NAs and providing no significant signal, the cells incubated with all NAs showed a  
21 clear MRI dark contrast (Figure 8B). When taking the control cells as a reference, we found an  
22 average darkening MRI contrast enhancement (ENH) of -80 %. This value is notably high given  
23 the low amount of SPIONs, which validates the strategy of assembling individual  
24 superparamagnetic nanoparticles around a larger fluorescent core to generate enhanced  
25 responses. The resulting supramolecular architecture, stabilized by additional polyelectrolytes,  
26 thus keeps the properties of the isolated units while offering novel ones thanks to the high  
27 density of associated functional units.  
28  
29  
30  
31  
32  
33  
34  
35  
36  
37  
38  
39  
40  
41  
42  
43  
44  
45  
46  
47  
48  
49  
50  
51  
52  
53  
54  
55  
56  
57  
58  
59  
60

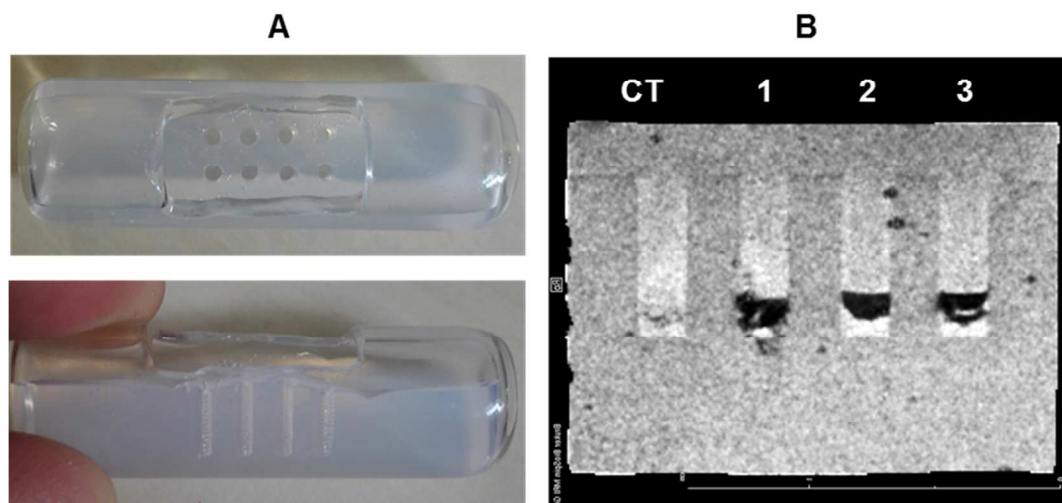
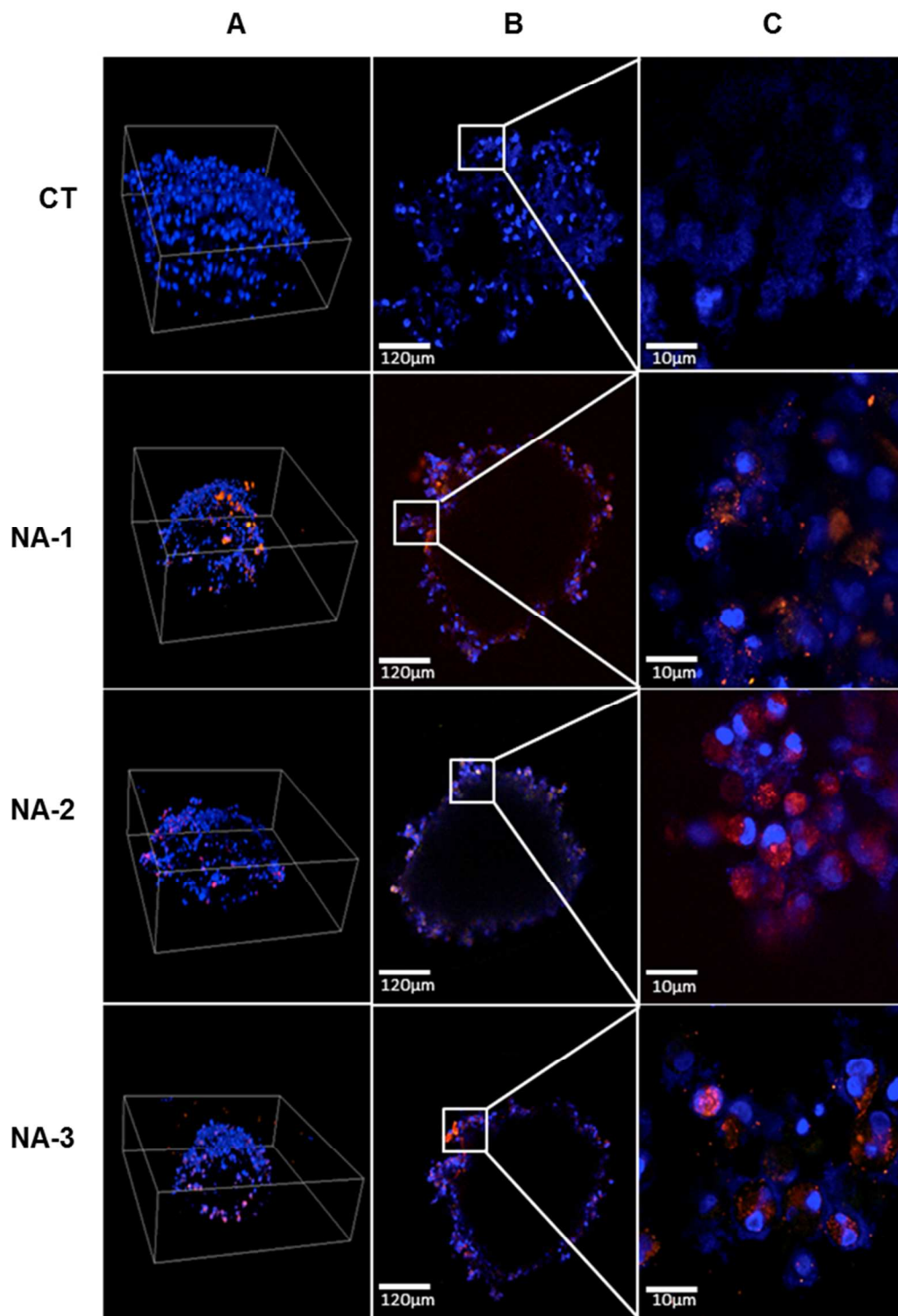


**Figure 8.** A) Home-made glass cylinder filled with 1% low-melting agarose gel displaying eight small wells dug with a plastic comb (top and lateral views). B) T2\* map MR images of Meso 11 control cells (CT), and cells incubated with magneto-fluorescent nanoassemblies NA-1, NA-2 and NA-3 for 24 h.

### Extension to labelling 3D cancer spheroids

Although biological investigations using cell monolayers represent the first compulsory step before envisaging any *in vivo* extensions, they still suffer from severe limitations, especially in the case of cancer treatment. First, the culture of cell monolayers is an artificial model that does not properly reproduce the growth and adhesion conditions of tumor cells *in vivo*. Second, solid tumors are made of compact cell clusters, preventing deep diffusion of the examined drugs. Hence, a novel culture mode of cells in three dimensions (3D), called multicellular tumor cell spheroid (MCTS), is nowadays boosting considerable attention to better apprehend the *in vivo* pathophysiological growing conditions<sup>62</sup> and generate 3D complex artificial tissues.<sup>63</sup> MCTS result from the assembling of  $2 \times 10^4$  cells, creating a spherical structure of densely packed cells with no adhesion on the surrounding culture material. Phenotype modifications are inevitably

1  
2  
3 induced and may considerably impact the cellular uptake mechanism. We thus elaborated MTCS  
4  
5 out of the Meso 11 mesothelioma cell lines and incubated them with a larger amount of magneto-  
6  
7 fluorescent nanoassemblies (40-60  $\mu\text{mol.L}^{-1}$  iron concentration) to take into account the high cell  
8  
9 density within the 3D cell arrangements. After usual washing steps and nucleus staining with  
10  
11 Hoechst, confocal fluorescence imaging was performed. Reconstituted images from Z-stack  
12  
13 acquisitions allowed us to visualize the compact spherical cell organization of MTCS and assess  
14  
15 their diameter to be around 400  $\mu\text{m}$ . Bright red-emissive spots could only be seen in the treated  
16  
17 spheroids, and could logically be assigned to the magneto-fluorescent nanoassemblies (Figure  
18  
19 9A). Due to the high cell density and large thickness of MTCS, no light transmission could pass  
20  
21 through (Figure S11), hence no emission could be collected out of the spheroid centre.  
22  
23 Therefore, the images of spheroid equatorial planes may be confusing as the cells in the middle  
24  
25 of the structure form a quenched black hole surrounded by a shell of labelled cells (Figure 9B).  
26  
27  
28  
29  
30  
31  
32  
33  
34  
35  
36  
37  
38  
39  
40  
41  
42  
43  
44  
45  
46  
47  
48  
49  
50  
51  
52  
53  
54  
55  
56  
57  
58  
59  
60



52  
53  
54  
55  
56  
57  
58  
59  
60

**Figure 9.** Confocal fluorescence imaging of Meso 11 MTCS ( $\sim 2 \times 10^4$  cells) incubated with magneto-fluorescent nanoassemblies NA-1, NA-2 and NA-3 for 24 h, and suspended in PBS solution. A) 3D reconstitutions of Z-multistack acquisitions. B) Sections of the spheroid

1  
2  
3 equatorial planes. C) Magnification of the peripheral shell of Meso 11 cells (blue emissive  
4  
5  
6 Hoechst-stained nuclei ( $\lambda_{\text{exc}} = 405 \text{ nm}$ ,  $\lambda_{\text{em}} = 425\text{-}475 \text{ nm}$ ), red-emissive magneto-fluorescent  
7  
8  
9 NAs ( $\lambda_{\text{exc}} = 488 \text{ nm}$ ,  $\lambda_{\text{em}} = 570\text{-}620 \text{ nm}$ ).

10  
11  
12 Magnification of the shell areas provides strong intracellular staining by all three kinds of  
13  
14 magneto-fluorescent NAs (Figure 9C). These quite remarkable images point out the fact that our  
15  
16 multimodal nanoassemblies are again well-internalized in self-assembled cells and represent  
17  
18 bright emissive nanotrackers without blurring the emission of other stained areas thanks to their  
19  
20 spot-like signals. Complementary MRI experiments following the same protocol as that  
21  
22 described above and using a T2\* sequence revealed again notable MRI negative contrast (Figure  
23  
24 S12). Compared to the experiments performed on free Meso 11 cells, the reduced response  
25  
26 originates from the nanotracker's uptake, limited to the periphery cells, as nicely illustrated by  
27  
28 confocal fluorescence imaging.  
29  
30  
31  
32  
33

34  
35 Before concluding these studies, a natural question arising from these investigations  
36  
37 relies on the biodegradability of FON@mag nanoassemblies to serve as future *in vivo* trackers. It  
38  
39 is worth recalling that their structure is based on the non-covalent association between three  
40  
41 components (a fluorescent core made of small self-assembled molecules, iron oxide  
42  
43 nanoparticles, and finally biodegradable polyelectrolytes) through electrostatic interactions,  
44  
45 hydrogen bonding or  $\pi$ - $\pi$  interactions. The absence of covalent linkage should thus easily lead to  
46  
47 the natural dissembling over time of all three components as already evidenced in a recent study,  
48  
49 hence biodegradability is ruled by each constitutive units. It turns out that iron oxide  
50  
51 nanoparticles have recently been proved, through systematic TEM investigations, to undergo  
52  
53 progressive destruction and assimilation by the "iron chain" involving ferritin (in charge of  
54  
55  
56  
57  
58  
59  
60

1  
2  
3 loading iron) and ferroportin (in charge of exporting iron) living media.<sup>6-7,64</sup> As for FONs, the  
4  
5 supramolecular association of their hydrophobic fluorophores, mainly driven by van der Waals  
6  
7 interactions and hydrogen bonding, progressively leads to the dissolution of the core into  
8  
9 individual molecules upon interaction with the lipid membrane of the endosomal/lysosomal  
10  
11 compartments where FONs or FON@mag accumulate.<sup>18,45-46</sup> Such dissolution could be  
12  
13 demonstrated through the dramatic fluorescence shift from red to greenish as a result of  
14  
15 differentiated surroundings of the solvatochromic fluorophores, which could only be explained  
16  
17 by changes in solvation and polarity as a result of FON dissociation. All these elements open  
18  
19 attractive potentialities for further *in vivo* use since biodegradability and not only  
20  
21 biocompatibility has nowadays become a mandatory criteria to meet.  
22  
23  
24  
25  
26  
27  
28  
29  
30

## 31 CONCLUSIONS

32  
33 In this study, we have demonstrated the modular fabrication of high-density core-shell magneto-  
34  
35 fluorescent nanoassemblies whose stabilizing external coating only takes place in a final step. In  
36  
37 this way, the incidence of the charge density, the chemical nature of the chelating anionic units,  
38  
39 the structure, the hydrophobicity and the length of the polyelectrolytes could be independently  
40  
41 studied without impacting the general core-shell architecture of the self-assembled magneto-  
42  
43 fluorescent probes. Long polyanionic chains ( $n \approx 50$  repetitive units) or block copolymers  
44  
45 revealed unsuccessful to stabilize the  $\sim 100$  nm-large nanoassemblies due to inter-assembly  
46  
47 bridging. By contrast, comb-like polyelectrolytes, comprising short anionic main chains ( $n \approx 25$   
48  
49 repetitive units) based on poly(methyl methacrylate, brought remarkable colloidal stability.  
50  
51 Interestingly, replacing acrylate units with phosphonate ones destroyed the shell of iron oxide  
52  
53  
54  
55  
56  
57  
58  
59  
60

1  
2  
3 nanoparticles around the FON core, leading to naked FONs. These results emphasize the clear  
4  
5 advantage of using polyelectrolytes instead of small anionic ligands thanks to their intrinsic  
6  
7 multifold attachment, provided that they do not exert detrimental competitive interactions with  
8  
9 the outer shell. Compared to conventional radical polymerization, RAFT-controlled radical  
10  
11 polymerization yielded polyelectrolytes with a narrow chain length dispersion. Incorporation of  
12  
13 alkyl RAFT agents induced local hydrophobic effects at the nanoassembly surface, generating a  
14  
15 more compact solvated structure. In this way, restricted water diffusion to the NA surface is  
16  
17 caused by the alkyl chains of the RAFT-controlled polyelectrolytes, which predominantly affects  
18  
19 the longitudinal relaxivity  $r_1$  of the resulting magneto-fluorescent nanoassemblies and provides  
20  
21 enhanced MRI contrast through  $r_2/r_1$  values as high as 21 at 60 MHz clinical frequency. The  
22  
23 lipophilicity and tight organization of the alkyl chains at the nanoassembly surface are also  
24  
25 suspected to influence the nanoassembly internalization rate in mesothelioma cancer cells, which  
26  
27 showed more progressive uptake without notable cytotoxicity. Labelling of MTCS, resulting  
28  
29 from the compaction of thousands of mesothelioma cancer cells could also be performed with all  
30  
31 nanoassemblies whose dual-mode MRI and fluorescence imaging capabilities were proved  
32  
33 effective. Further investigations on these magneto-fluorescent nanoassemblies displaying easily  
34  
35 tunable surface modification are under way to gain insight into the uptake mechanism, *in vivo*  
36  
37 distribution and biodegradation as a function of the polyelectrolyte coating that requires accurate  
38  
39 control, like those issued from RAFT polymerization, before any clinical transfer can be  
40  
41 envisaged.  
42  
43  
44  
45  
46  
47  
48  
49  
50  
51  
52  
53  
54  
55  
56  
57  
58  
59  
60

## EXPERIMENTAL SECTION

### Polymer synthesis and characterizations

*Materials.* Azobisisobutyronitrile (AIBN; Sigma-Aldrich; 98 %) was recrystallized twice from methanol prior to use. [(2-methylacryloyl)oxy]methyl phosphonic acid (MAPA) was purchased from Specific Polymers (“MPAC1 Acid”) and used as received. Poly(acrylic acid) (PAA) (average  $M_n$  1800  $\text{g}\cdot\text{mol}^{-1}$ ), poly(ethylene glycol) methyl ether methacrylate (average  $M_n$  1100, and average  $M_n$  2000  $\text{g}\cdot\text{mol}^{-1}$  at 50 wt. % in  $\text{H}_2\text{O}$ ; MAPEG<sub>1100</sub> and MAPEG<sub>2000</sub>, respectively), methacrylic acid (MAA; 99 %) and 2-cyano-2-propyl dodecyl trithiocarbonate (CPDTC; 97 %) were purchased from Sigma-Aldrich and used as received. Polymethacrylic acid (PMMA) homopolymer TP942 ( $M_w = 6218\text{g}\cdot\text{mol}^{-1}$ ,  $M_n = 2609 \text{g}\cdot\text{mol}^{-1}$ ) was purchased from Coatex Company. Poly(ethylene glycol) methyl ether (PEG<sub>2000</sub>) ( $M_w = 2000 \text{g}\cdot\text{mol}^{-1}$ ) was purchased from Clarian Co, LTD. Methanol (Fischer; 99.5 %) was used as received. N,N-dimethylformamide (DMF; Alfa Aesar; 99.8 %) was distilled under reduced pressure over  $\text{CaH}_2$  prior to use.

*Synthesis of PMAA-g-PEG<sub>2000</sub> (2).* 50 g of PMMA were placed in a four-neck flask and mixed with 0.34 g of a 50 wt. % NaOH solution (corresponding to 2.5 mole % of PMMA carboxylic functions). To the medium were added 95.76 g (corresponding to 29 mole % of PMMA carboxylic functions) of PEG<sub>2000</sub> and the reaction mixture was heated to 80°C and gradually placed under vacuum (~ 50 mbar). After distillation of water, the temperature of the reaction mixture was gradually increased to 175°C. The reaction time was measured from the moment on the reaction medium reached 170° C. The reaction was continued for a further 4 h. After completion of the reaction, the reaction vessel was returned to atmospheric pressure and the heat turned off. Once the temperature of the reaction mixture reached 90°C, the melted

1  
2  
3 polymer was diluted to 50 wt. % in water. The polymer was purified by dialysis against distilled  
4 water using a dialysis membrane with 3500–5000 molecular weight cut-off (Spectra/Por<sup>®</sup>2,  
5 Spectrum Medical Industries, Inc., CA, USA) at 20°C. The polymer was obtained after  
6 lyophilization. The yield of the esterification reaction was controlled by measuring the acidic  
7 index before and after the reaction. The grafting efficiency was evaluated to be 23 % by  
8 determining the unreacted carboxylic acid content of coupling polymer with an acid-base  
9 titration technique.  
10  
11

12  
13  
14  
15  
16  
17  
18  
19  
20 *Synthesis of poly(MAA-stat-MAPEG<sub>2000</sub>) (3).* The targeted molar fraction in MAA was 80  
21 %. 14 mg of AIBN ( $8.5 \times 10^{-2}$  mmol), 55.5 mg of CPDTC ( $1.61 \times 10^{-2}$  mmol), 344 mg of MAA  
22 (4.00 mmol), 2.0 mL of methanol and 4.00 g of the solution of MAPEG<sub>2000</sub> at 50 wt. % in water  
23 (1.00 mmol) were added in this order into a dried Schlenk flask. The solution was thoroughly  
24 deoxygenated by four freeze-pump-thaw cycles. The flask was filled with nitrogen gas and  
25 placed in an oil bath maintained at 70 °C for 24 h under magnetic stirring. The solvents were  
26 then evaporated under reduced pressure. Analysis by <sup>1</sup>H NMR confirmed the almost total  
27 conversion of the methacrylate functional groups (> 99 %). The molecular weight of the sample  
28 was determined by size exclusion chromatography in DMF.  
29  
30  
31  
32  
33  
34  
35  
36  
37  
38  
39

40  
41 *Synthesis of poly(MAPA-stat-MAPEG<sub>1100</sub>) (4).* Two samples were synthesized, with  
42 targeted molar fractions of MAPA of either 20 % or 60 %. For the synthesis of the former, 3.9  
43 mg of AIBN (0.25 eq.), 32.6 mg of CPDTC ( $9.44 \times 10^{-2}$  mmol, 1 eq.), 85.0 mg of MAPA (5 eq.),  
44 2.0768 g of MAPEG<sub>1100</sub> (20 eq.) and 5.0 mL of DMF were added in this order into a dried  
45 Schlenk flask. The solution was thoroughly deoxygenated by four freeze-pump-thaw cycles. The  
46 flask was filled with nitrogen gas and placed in an oil bath maintained at 70 °C for 24 h under  
47 magnetic stirring. The solvent was then evaporated under reduced pressure. The experimental  
48  
49  
50  
51  
52  
53  
54  
55  
56  
57  
58  
59  
60

1  
2  
3 procedure was the same for the synthesis of the second sample, with the following proportions  
4  
5 for the reactants: 7.8 mg of AIBN (0.25 eq.), 65.3 mg of CPDTC ( $1.89 \times 10^{-1}$  mmol, 1 eq.), 510.0  
6  
7 mg of MAPA (15 eq.), 2.0768 g of MAPEG<sub>1100</sub> (10 eq.) and 5.0 mL of DMF. Analysis by <sup>1</sup>H  
8  
9 NMR confirmed the almost total conversion of the methacrylate functional groups (> 99 %). The  
10  
11 molecular weights of the samples were determined by size exclusion chromatography in DMF.  
12  
13

14  
15 *SEC polymer characterizations.* Molecular weights were determined by size exclusion  
16  
17 chromatography in DMF containing LiBr at a concentration of 10 mmol.L<sup>-1</sup>. Solutions of  
18  
19 samples with concentrations around 5 mg.mL<sup>-1</sup> were prepared and filtered (PTFE membrane;  
20  
21 0.20 μm) before injection. The flow rate was 0.9 mL.min<sup>-1</sup> (50 °C). The following Agilent 1260  
22  
23 Infinity series setup was used: a G1310B isocratic pump; a G1322A degasser; a G1329B auto-  
24  
25 sampler; a G1316A thermostated column compartment equipped with set of Polymer  
26  
27 Laboratories PLgel columns (nominal particle size: 5 μm) composed of a guard column (50×7.5  
28  
29 mm) and two MIXED-D columns (300×7.5 mm); a G1314B variable wavelength detector; a  
30  
31 G7800A multidetector suite equipped with a MDS refractive index detector. Calibration was  
32  
33 performed using a set of EasiVial polystyrene PS-M standards. Agilent GPC/SEC software and  
34  
35 multi-detector upgrade were used to determine molar mass values and distributions.  
36  
37  
38  
39  
40  
41

### 42 **Fabrication and structural characterizations of polyelectrolyte-coated nanoassemblies**

43  
44 *Nanoassembly fabrication.* A solution of phosphonic acid fluorophores,<sup>17</sup> dissolved in THF  
45  
46 (50 μL, 0.1 wt. %) was added under vigorous stirring to a solution of maghemite nanoparticles in  
47  
48 nitric acid (2.5 mL, 0.006 wt. %, pH = 1.2). After a few seconds, the magneto-fluorescent NAs  
49  
50 were formed. The polyelectrolyte of interest was added as a powder (added amount for PAA (1):  
51  
52 5 mg, PMAA-g-PEG (2): 17 mg, and poly(MAA-*stat*-MAPEG) (3): 18 mg) and then,  
53  
54 ammonium hydroxide (1 mol.L<sup>-1</sup>) was added dropwise under stirring until pH = 9 was reached.  
55  
56  
57  
58  
59  
60

1  
2  
3 The resulting translucent solution was allowed to stir for a further 30 min and dialyzed using a  
4 Spectra Por membrane (Standard Grade Regenerated Cellulose; cut-off: 8-10 kDa for PAA (1),  
5 and 300 kDa for (2) and (3) against Millipore water (600 mL) over 24 h to remove the excess of  
6 polymers and get neutral pH. The resulting solution was spread into small vials (2 mL content)  
7 and lyophilized. The vials were finally stored at -18 °C until solution reconstitution with water,  
8 PBS or cell culture medium.  
9  
10  
11  
12  
13  
14  
15  
16

17 *DLS characterizations.* The hydrodynamic diameter  $D_H$  and size dispersion of the nano-  
18 objects were determined by dynamic light scattering (DLS) by means of a nanoparticle size  
19 analyzer Cordouan (Vasco 3) equipped with a 40 mW diode laser operating at 658 nm.  
20 Measurements were collected in a backscattering mode at an angle of 135°. Measurements were  
21 carried out at 25 °C on aqueous solutions of NPs. For each sample, intensity measurements were  
22 carried out in a multi-acquisition mode implying automatically adjusted correlograms, and  
23 averaged measurements on 6 acquisitions. Nanoparticle mean sizes and distribution widths were  
24 obtained by fitting each correlogram with a Cumulants algorithm. Measurements of surface  
25 potential  $\zeta$  were carried out by means of a Zetasizer Nano ZS ZEN 3600 (Malvern). The samples  
26 were placed in quartz cells. Several measurements were realized for each sample according to a  
27 predefined operating procedure.  
28  
29  
30  
31  
32  
33  
34  
35  
36  
37  
38  
39  
40  
41  
42

43 *TEM analyses.* Nanoparticle morphology was investigated by transmission electron  
44 microscopy (MO-Jeol 123S0 (80 kV)). All NA solutions were deposited onto holey carbon-  
45 coated copper grids (300 mesh).  
46  
47  
48  
49  
50

## 51 **Steady-state and time-resolved fluorescence measurements**

52 *Steady-state fluorescence measurements.* UV-visible absorption spectra were recorded  
53 using a Varian Model Cary 5E spectrophotometer equipped with an integrating sphere DRA  
54  
55  
56  
57  
58  
59  
60

1  
2  
3 2500. Fluorolog 2 spectrofluorimeter was used (Jobin-Yvon/Horiba). Correction for the emission  
4 spectra with regard to the spectral response of the detector was automatically applied.  
5  
6 Fluorescence quantum yields were determined in solution, referred to coumarine 540 A in EtOH  
7  
8 ( $\Phi_f = 0.38$ ).<sup>65</sup>  
9

10  
11  
12 *Time-resolved fluorescence measurements.* Fluorescence time decays were measured in  
13 water using the fully automated spectrofluorimeter (model Fluotime 300, PicoQuant) following  
14 the time-correlated photon counting method. Excitation was performed using a pulsed laser  
15 diode (LDH-D-C-450B) working at  $450 \pm 10$  nm with a 70 ps full width at half maximum. The  
16 excitation and emission polarizers were set in the vertical position and at the magic angle ( $54.7^\circ$ )  
17 respectively to get polarization-independent fluorescence signals. Fluorescence decays were  
18 recorded using a Hybrid-PMT detector combined with an acquisition temporal resolution up to  
19 25 ps. A 473 nm Notch filter (BPL01-473R-25) purchased from Semrock was used to discard  
20 any possible contribution of excitation light scattering).  
21  
22  
23  
24  
25  
26  
27  
28  
29  
30  
31  
32

### 33 34 35 **Static and dynamic magnetic measurements**

36  
37 *Magnetization measurements.* Magnetic measurements were collected with a Quantum  
38 Design MPMS-5S SQUID magnetometer. All magnetic measurements were performed on dry  
39 powders. The samples were pressed into pellets in order to prevent nanocrystal orientation under  
40 the external magnetic field. The magnetization curves were measured at 2.5 K and 310 K from  
41 +50 kOe to -50 kOe. All data were corrected for diamagnetic contribution due to the sample  
42 holder which was separately measured. The thermal dependence of magnetization was recorded  
43 from 10 to 300 K upon zero-field-cooling (ZFC) and field-cooling (FC) conditions. ZFC  
44 magnetizations were measured by cooling samples in a zero magnetic field and then by  
45  
46  
47  
48  
49  
50  
51  
52  
53  
54  
55  
56  
57  
58  
59  
60

1  
2  
3 increasing the temperature in the presence of a 50 Oe magnetic field, whereas field-cooled (FC)  
4 curves were recorded by cooling the samples in the same probe field at 50 Oe.  
5  
6

7  
8 *NMR relaxometry measurements.* Measurements of  $^1\text{H}$  NMR longitudinal ( $T_1$ ) and  
9 transverse ( $T_2$ ) relaxation times were performed at room temperature on sample solutions diluted  
10 with water in the range  $0.01 \text{ MHz} \leq \nu \leq 60 \text{ MHz}$  frequency range. Generation and detection of  
11 the NMR signal involved a Smartracer Stellar relaxometer (using the Fast-Field-Cycling  
12 technique) for  $\nu \leq 10 \text{ MHz}$ , and a Stellar Spinmaster spectrometer for  $\nu > 10 \text{ MHz}$ . For the very  
13 low field range ( $\nu < 3.2 \text{ MHz}$  for  $T_1$  and  $\nu < 4 \text{ MHz}$  for  $T_2$ ), ad hoc pre-polarized sequences were  
14 used to increase the NMR proton signal. In the second case, the standard radio frequency  
15 excitation sequences Carr-Purcell-Meiboom-Gill (CPMG)-like ( $T_2$ ) and saturation recovery ( $T_1$ )  
16 were used. The efficiency of samples as MRI contrast agents was determined from the measured  
17  $T_1$  and  $T_2$  by calculating the nuclear longitudinal  $r_1$  and transverse  $r_2$  relaxivities as given by:  
18  
19  
20  
21  
22  
23  
24  
25  
26  
27  
28  
29  
30  
31

$$r_i = \frac{(1/T_i)_{\text{meas}} - (1/T_i)_{\text{dia}}}{c_{\text{Fe}}}$$

32  
33  
34  
35  
36  
37 where  $(1/T_i)_{\text{meas}}$  is the measured relaxation rate,  $(1/T_i)_{\text{dia}}$  the diamagnetic contribution of  
38 Millipore water ( $\sim 4 \text{ s}^{-1}$ ), and  $c_{\text{Fe}}$  the iron concentration in  $\text{mmol.L}^{-1}$  for each sample.  
39  
40  
41

42 *Photophysical characterizations.* UV-visible absorption spectra were recorded using a  
43 Varian Model Cary 5E spectrophotometer equipped with an integrating sphere DRA 2500.  
44 Fluorolog 2 spectrofluorimeter was used (Jobin-Yvon/Horiba). Correction for the emission  
45 spectra with regard to the spectral response of the detector was automatically applied.  
46  
47  
48  
49  
50  
51  
52  
53  
54  
55  
56  
57  
58  
59  
60  
61  
62  
63  
64  
65  
66  
67  
68  
69  
70  
71  
72  
73  
74  
75  
76  
77  
78  
79  
80  
81  
82  
83  
84  
85  
86  
87  
88  
89  
90  
91  
92  
93  
94  
95  
96  
97  
98  
99  
100  
101  
102  
103  
104  
105  
106  
107  
108  
109  
110  
111  
112  
113  
114  
115  
116  
117  
118  
119  
120  
121  
122  
123  
124  
125  
126  
127  
128  
129  
130  
131  
132  
133  
134  
135  
136  
137  
138  
139  
140  
141  
142  
143  
144  
145  
146  
147  
148  
149  
150  
151  
152  
153  
154  
155  
156  
157  
158  
159  
160  
161  
162  
163  
164  
165  
166  
167  
168  
169  
170  
171  
172  
173  
174  
175  
176  
177  
178  
179  
180  
181  
182  
183  
184  
185  
186  
187  
188  
189  
190  
191  
192  
193  
194  
195  
196  
197  
198  
199  
200  
201  
202  
203  
204  
205  
206  
207  
208  
209  
210  
211  
212  
213  
214  
215  
216  
217  
218  
219  
220  
221  
222  
223  
224  
225  
226  
227  
228  
229  
230  
231  
232  
233  
234  
235  
236  
237  
238  
239  
240  
241  
242  
243  
244  
245  
246  
247  
248  
249  
250  
251  
252  
253  
254  
255  
256  
257  
258  
259  
260  
261  
262  
263  
264  
265  
266  
267  
268  
269  
270  
271  
272  
273  
274  
275  
276  
277  
278  
279  
280  
281  
282  
283  
284  
285  
286  
287  
288  
289  
290  
291  
292  
293  
294  
295  
296  
297  
298  
299  
300  
301  
302  
303  
304  
305  
306  
307  
308  
309  
310  
311  
312  
313  
314  
315  
316  
317  
318  
319  
320  
321  
322  
323  
324  
325  
326  
327  
328  
329  
330  
331  
332  
333  
334  
335  
336  
337  
338  
339  
340  
341  
342  
343  
344  
345  
346  
347  
348  
349  
350  
351  
352  
353  
354  
355  
356  
357  
358  
359  
360  
361  
362  
363  
364  
365  
366  
367  
368  
369  
370  
371  
372  
373  
374  
375  
376  
377  
378  
379  
380  
381  
382  
383  
384  
385  
386  
387  
388  
389  
390  
391  
392  
393  
394  
395  
396  
397  
398  
399  
400  
401  
402  
403  
404  
405  
406  
407  
408  
409  
410  
411  
412  
413  
414  
415  
416  
417  
418  
419  
420  
421  
422  
423  
424  
425  
426  
427  
428  
429  
430  
431  
432  
433  
434  
435  
436  
437  
438  
439  
440  
441  
442  
443  
444  
445  
446  
447  
448  
449  
450  
451  
452  
453  
454  
455  
456  
457  
458  
459  
460  
461  
462  
463  
464  
465  
466  
467  
468  
469  
470  
471  
472  
473  
474  
475  
476  
477  
478  
479  
480  
481  
482  
483  
484  
485  
486  
487  
488  
489  
490  
491  
492  
493  
494  
495  
496  
497  
498  
499  
500  
501  
502  
503  
504  
505  
506  
507  
508  
509  
510  
511  
512  
513  
514  
515  
516  
517  
518  
519  
520  
521  
522  
523  
524  
525  
526  
527  
528  
529  
530  
531  
532  
533  
534  
535  
536  
537  
538  
539  
540  
541  
542  
543  
544  
545  
546  
547  
548  
549  
550  
551  
552  
553  
554  
555  
556  
557  
558  
559  
560  
561  
562  
563  
564  
565  
566  
567  
568  
569  
570  
571  
572  
573  
574  
575  
576  
577  
578  
579  
580  
581  
582  
583  
584  
585  
586  
587  
588  
589  
590  
591  
592  
593  
594  
595  
596  
597  
598  
599  
600  
601  
602  
603  
604  
605  
606  
607  
608  
609  
610  
611  
612  
613  
614  
615  
616  
617  
618  
619  
620  
621  
622  
623  
624  
625  
626  
627  
628  
629  
630  
631  
632  
633  
634  
635  
636  
637  
638  
639  
640  
641  
642  
643  
644  
645  
646  
647  
648  
649  
650  
651  
652  
653  
654  
655  
656  
657  
658  
659  
660  
661  
662  
663  
664  
665  
666  
667  
668  
669  
670  
671  
672  
673  
674  
675  
676  
677  
678  
679  
680  
681  
682  
683  
684  
685  
686  
687  
688  
689  
690  
691  
692  
693  
694  
695  
696  
697  
698  
699  
700  
701  
702  
703  
704  
705  
706  
707  
708  
709  
710  
711  
712  
713  
714  
715  
716  
717  
718  
719  
720  
721  
722  
723  
724  
725  
726  
727  
728  
729  
730  
731  
732  
733  
734  
735  
736  
737  
738  
739  
740  
741  
742  
743  
744  
745  
746  
747  
748  
749  
750  
751  
752  
753  
754  
755  
756  
757  
758  
759  
760  
761  
762  
763  
764  
765  
766  
767  
768  
769  
770  
771  
772  
773  
774  
775  
776  
777  
778  
779  
780  
781  
782  
783  
784  
785  
786  
787  
788  
789  
790  
791  
792  
793  
794  
795  
796  
797  
798  
799  
800  
801  
802  
803  
804  
805  
806  
807  
808  
809  
810  
811  
812  
813  
814  
815  
816  
817  
818  
819  
820  
821  
822  
823  
824  
825  
826  
827  
828  
829  
830  
831  
832  
833  
834  
835  
836  
837  
838  
839  
840  
841  
842  
843  
844  
845  
846  
847  
848  
849  
850  
851  
852  
853  
854  
855  
856  
857  
858  
859  
860  
861  
862  
863  
864  
865  
866  
867  
868  
869  
870  
871  
872  
873  
874  
875  
876  
877  
878  
879  
880  
881  
882  
883  
884  
885  
886  
887  
888  
889  
890  
891  
892  
893  
894  
895  
896  
897  
898  
899  
900  
901  
902  
903  
904  
905  
906  
907  
908  
909  
910  
911  
912  
913  
914  
915  
916  
917  
918  
919  
920  
921  
922  
923  
924  
925  
926  
927  
928  
929  
930  
931  
932  
933  
934  
935  
936  
937  
938  
939  
940  
941  
942  
943  
944  
945  
946  
947  
948  
949  
950  
951  
952  
953  
954  
955  
956  
957  
958  
959  
960  
961  
962  
963  
964  
965  
966  
967  
968  
969  
970  
971  
972  
973  
974  
975  
976  
977  
978  
979  
980  
981  
982  
983  
984  
985  
986  
987  
988  
989  
990  
991  
992  
993  
994  
995  
996  
997  
998  
999  
1000  
1001  
1002  
1003  
1004  
1005  
1006  
1007  
1008  
1009  
1010  
1011  
1012  
1013  
1014  
1015  
1016  
1017  
1018  
1019  
1020  
1021  
1022  
1023  
1024  
1025  
1026  
1027  
1028  
1029  
1030  
1031  
1032  
1033  
1034  
1035  
1036  
1037  
1038  
1039  
1040  
1041  
1042  
1043  
1044  
1045  
1046  
1047  
1048  
1049  
1050  
1051  
1052  
1053  
1054  
1055  
1056  
1057  
1058  
1059  
1060  
1061  
1062  
1063  
1064  
1065  
1066  
1067  
1068  
1069  
1070  
1071  
1072  
1073  
1074  
1075  
1076  
1077  
1078  
1079  
1080  
1081  
1082  
1083  
1084  
1085  
1086  
1087  
1088  
1089  
1090  
1091  
1092  
1093  
1094  
1095  
1096  
1097  
1098  
1099  
1100  
1101  
1102  
1103  
1104  
1105  
1106  
1107  
1108  
1109  
1110  
1111  
1112  
1113  
1114  
1115  
1116  
1117  
1118  
1119  
1120  
1121  
1122  
1123  
1124  
1125  
1126  
1127  
1128  
1129  
1130  
1131  
1132  
1133  
1134  
1135  
1136  
1137  
1138  
1139  
1140  
1141  
1142  
1143  
1144  
1145  
1146  
1147  
1148  
1149  
1150  
1151  
1152  
1153  
1154  
1155  
1156  
1157  
1158  
1159  
1160  
1161  
1162  
1163  
1164  
1165  
1166  
1167  
1168  
1169  
1170  
1171  
1172  
1173  
1174  
1175  
1176  
1177  
1178  
1179  
1180  
1181  
1182  
1183  
1184  
1185  
1186  
1187  
1188  
1189  
1190  
1191  
1192  
1193  
1194  
1195  
1196  
1197  
1198  
1199  
1200  
1201  
1202  
1203  
1204  
1205  
1206  
1207  
1208  
1209  
1210  
1211  
1212  
1213  
1214  
1215  
1216  
1217  
1218  
1219  
1220  
1221  
1222  
1223  
1224  
1225  
1226  
1227  
1228  
1229  
1230  
1231  
1232  
1233  
1234  
1235  
1236  
1237  
1238  
1239  
1240  
1241  
1242  
1243  
1244  
1245  
1246  
1247  
1248  
1249  
1250  
1251  
1252  
1253  
1254  
1255  
1256  
1257  
1258  
1259  
1260  
1261  
1262  
1263  
1264  
1265  
1266  
1267  
1268  
1269  
1270  
1271  
1272  
1273  
1274  
1275  
1276  
1277  
1278  
1279  
1280  
1281  
1282  
1283  
1284  
1285  
1286  
1287  
1288  
1289  
1290  
1291  
1292  
1293  
1294  
1295  
1296  
1297  
1298  
1299  
1300  
1301  
1302  
1303  
1304  
1305  
1306  
1307  
1308  
1309  
1310  
1311  
1312  
1313  
1314  
1315  
1316  
1317  
1318  
1319  
1320  
1321  
1322  
1323  
1324  
1325  
1326  
1327  
1328  
1329  
1330  
1331  
1332  
1333  
1334  
1335  
1336  
1337  
1338  
1339  
1340  
1341  
1342  
1343  
1344  
1345  
1346  
1347  
1348  
1349  
1350  
1351  
1352  
1353  
1354  
1355  
1356  
1357  
1358  
1359  
1360  
1361  
1362  
1363  
1364  
1365  
1366  
1367  
1368  
1369  
1370  
1371  
1372  
1373  
1374  
1375  
1376  
1377  
1378  
1379  
1380  
1381  
1382  
1383  
1384  
1385  
1386  
1387  
1388  
1389  
1390  
1391  
1392  
1393  
1394  
1395  
1396  
1397  
1398  
1399  
1400  
1401  
1402  
1403  
1404  
1405  
1406  
1407  
1408  
1409  
1410  
1411  
1412  
1413  
1414  
1415  
1416  
1417  
1418  
1419  
1420  
1421  
1422  
1423  
1424  
1425  
1426  
1427  
1428  
1429  
1430  
1431  
1432  
1433  
1434  
1435  
1436  
1437  
1438  
1439  
1440  
1441  
1442  
1443  
1444  
1445  
1446  
1447  
1448  
1449  
1450  
1451  
1452  
1453  
1454  
1455  
1456  
1457  
1458  
1459  
1460  
1461  
1462  
1463  
1464  
1465  
1466  
1467  
1468  
1469  
1470  
1471  
1472  
1473  
1474  
1475  
1476  
1477  
1478  
1479  
1480  
1481  
1482  
1483  
1484  
1485  
1486  
1487  
1488  
1489  
1490  
1491  
1492  
1493  
1494  
1495  
1496  
1497  
1498  
1499  
1500  
1501  
1502  
1503  
1504  
1505  
1506  
1507  
1508  
1509  
1510  
1511  
1512  
1513  
1514  
1515  
1516  
1517  
1518  
1519  
1520  
1521  
1522  
1523  
1524  
1525  
1526  
1527  
1528  
1529  
1530  
1531  
1532  
1533  
1534  
1535  
1536  
1537  
1538  
1539  
1540  
1541  
1542  
1543  
1544  
1545  
1546  
1547  
1548  
1549  
1550  
1551  
1552  
1553  
1554  
1555  
1556  
1557  
1558  
1559  
1560  
1561  
1562  
1563  
1564  
1565  
1566  
1567  
1568  
1569  
1570  
1571  
1572  
1573  
1574  
1575  
1576  
1577  
1578  
1579  
1580  
1581  
1582  
1583  
1584  
1585  
1586  
1587  
1588  
1589  
1590  
1591  
1592  
1593  
1594  
1595  
1596  
1597  
1598  
1599  
1600  
1601  
1602  
1603  
1604  
1605  
1606  
1607  
1608  
1609  
1610  
1611  
1612  
1613  
1614  
1615  
1616  
1617  
1618  
1619  
1620  
1621  
1622  
1623  
1624  
1625  
1626  
1627  
1628  
1629  
1630  
1631  
1632  
1633  
1634  
1635  
1636  
1637  
1638  
1639  
1640  
1641  
1642  
1643  
1644  
1645  
1646  
1647  
1648  
1649  
1650  
1651  
1652  
1653  
1654  
1655  
1656  
1657  
1658  
1659  
1660  
1661  
1662  
1663  
1664  
1665  
1666  
1667  
1668  
1669  
1670  
1671  
1672  
1673  
1674  
1675  
1676  
1677  
1678  
1679  
1680  
1681  
1682  
1683  
1684  
1685  
1686  
1687  
1688  
1689  
1690  
1691  
1692  
1693  
1694  
1695  
1696  
1697  
1698  
1699  
1700  
1701  
1702  
1703  
1704  
1705  
1706  
1707  
1708  
1709  
1710  
1711  
1712  
1713  
1714  
1715  
1716  
1717  
1718  
1719  
1720  
1721  
1722  
1723  
1724  
1725  
1726  
1727  
1728  
1729  
1730  
1731  
1732  
1733  
1734  
1735  
1736  
1737  
1738  
1739  
1740  
1741  
1742  
1743  
1744  
1745  
1746  
1747  
1748  
1749  
1750  
1751  
1752  
1753  
1754  
1755  
1756  
1757  
1758  
1759  
1760  
1761  
1762  
1763  
1764  
1765  
1766  
1767  
1768  
1769  
1770  
1771  
1772  
1773  
1774  
1775  
1776  
1777  
1778  
1779  
1780  
1781  
1782  
1783  
1784  
1785  
1786  
1787  
1788  
1789  
1790  
1791  
1792  
1793  
1794  
1795  
1796  
1797  
1798  
1799  
1800  
1801  
1802  
1803  
1804  
1805  
1806  
1807  
1808  
1809  
1810  
1811  
1812  
1813  
1814  
1815  
1816  
1817  
1818  
1819  
1820  
1821  
1822  
1823  
1824  
1825  
1826  
1827  
1828  
1829  
1830  
1831  
1832  
1833  
1834  
1835  
1836  
1837  
1838  
1839  
1840  
1841  
1842  
1843  
1844  
1845  
1846  
1847  
1848  
1849  
1850  
1851  
1852  
1853  
1854  
1855  
1856  
1857  
1858  
1859  
1860  
1861  
1862  
1863  
1864  
1865  
1866  
1867  
1868  
1869  
1870  
1871  
1872  
1873  
1874  
1875  
1876  
1877  
1878  
1879  
1880  
1881  
1882  
1883  
1884  
1885  
1886  
1887  
1888  
1889  
1890  
1891  
1892  
1893  
1894  
1895  
1896  
1897  
1898  
1899  
1900  
1901  
1902  
1903  
1904  
1905  
1906  
1907  
1908  
1909  
1910  
1911  
1912  
1913  
1914  
1915  
1916  
1917  
1918  
1919  
1920  
1921  
1922  
1923  
1924  
1925  
1926  
1927  
1928  
1929  
1930  
1931  
1932  
1933  
1934  
1935  
1936  
1937  
1938  
1939  
1940  
1941  
1942  
1943  
1944  
1945  
1946  
1947  
1948  
1949  
1950  
1951  
1952  
1953  
1954  
1955  
1956  
1957  
1958  
1959  
1960  
1961  
1962  
1963  
1964  
1965  
1966  
1967  
1968  
1969  
1970  
1971  
1972  
1973  
1974  
1975  
1976  
1977  
1978  
1979  
1980  
1981  
1982  
1983  
1984  
1985  
1986  
1987  
1988  
1989  
1990  
1991  
1992  
1993  
1994  
1995  
1996  
1997  
1998  
1999  
2000  
2001  
2002  
2003  
2004  
2005  
2006  
2007  
2008  
2009  
2010  
2011  
2012  
2013  
2014  
2015  
2016  
2017  
2018  
2019  
2020  
2021  
2022  
2023  
2024  
2025  
2026  
2027  
2028  
2029  
2030  
2031  
2032  
2033  
2034  
2035  
2036  
2037  
2038  
2039  
2040  
2041  
2042  
2043  
2044  
2045  
2046  
2047  
2048  
2049  
2050  
2051  
2052  
2053  
2054  
2055  
2056  
2057  
2058  
2059  
2060  
2061  
2062  
2063  
2064  
2065  
2066  
2067  
2068  
2069  
2070  
2071  
2072  
2073  
2074  
2075  
2076  
2077  
2078  
2079  
2080  
2081  
2082  
2083  
2084  
2085  
2086  
2087  
2088  
2089  
2090  
2091  
2092  
2093  
2094  
2095  
2096  
2097  
2098  
2099  
2100  
2101  
2102  
2103  
2104  
2105  
2106  
2107  
2108

## Cell culture, internalization and bioimaging

*Cell culture.* The mesothelioma cell line Meso 11 was established from pleural fluids of patients. All cells were maintained in RPMI medium (Invitrogen) supplemented with 2 mmol.L<sup>-1</sup> glutamine, 100 IU/mL penicillin, 0.1 mg.mL<sup>-1</sup> streptomycin and 10 % heat-inactivated foetal calf serum(FCS)(Eurobio), and grown in a humidified atmosphere of 37 °C and 5 % CO<sub>2</sub>. For all experiments, the cell cultures at a confluence of about 80–90 % were washed once with phosphate buffered saline (PBS) and trypsinized (0.05 % trypsin/0.02 % EDTA)(Invitrogen) for 5 minutes. The cells were re-suspended in culture medium and eosin was used to determine viability before seeding.

*Three-dimensional (3D) spheroid culture.* Meso 11 cells were seeded into Nunclon Sphera 96-well microplate (Thermoscientific) at a density of 2×10<sup>4</sup> cells/well in 180 μL of culture medium. Cells were centrifuged at 800 G for 1 minute. After 48 h of incubation at 37°C and 5 % CO<sub>2</sub>, the 3D spheroid structure was established.

*Flow cytometry studies.* Meso 11 cells were seeded on a 6-well plate at 2×10<sup>5</sup> cells per well. After 24 h, solutions of NA-1, NA-2 and NA-3 (final iron concentration of 3.3 μmol.L<sup>-1</sup>, 2.6 μmol.L<sup>-1</sup> and 2.09 μmol.L<sup>-1</sup>) were added and let in contact for 30, 60, 120, 240, 360, 960 and 1440 minutes. Then, each well was washed with PBS and incubated with 300 μL of trypsin/EDTA for 5 minutes. 700 μL of culture medium were added and the cell suspensions were centrifuged at 800 G for 5 minutes. The cell pellets were re-suspended in PBS (50 μL) containing Zombie NIR® (Biolegend) diluted at 1/50 and incubated 30 minutes at room temperature. Analyses were performed using an ImageStreamX Imaging Flow Cytometer (Amnis Corporation, Seattle, WA) equipped with INSPIRE software. A 40× magnification was used for all samples. 10<sup>4</sup> living cells were analyzed for each conditions. Data analysis was

1  
2  
3 performed using the IDEAS software (Amnis Corporation). The nanoassemblies and Zombie  
4 NIR® were excited with a 488 nm ion-argon laser (power 100 mW). Fluorescence signals of the  
5 nanoassemblies and Zombie NIR® were collected on channel 3 (560-595 nm and channel 12  
6 (745-800 nm), respectively. Intensity-adjusted brightfield images were collected on channel 1  
7 (430-480 nm). The gating strategy for analysis involved the selection of focused live cells first  
8 on viability marker, then on the nanoassembly fluorescence.  
9  
10  
11  
12  
13  
14  
15  
16

17 *Cell monolayer fixation and TEM imaging.* Meso 11 cells were seeded on a 6-well plate at  
18  $5 \times 10^5$  cells per well. After 24 h, solutions of **NA-1**, **NA-2** and **NA-3** (final iron concentration of  
19  $3.3 \mu\text{mol.L}^{-1}$ ,  $2.6 \mu\text{mol.L}^{-1}$  and  $2.09 \mu\text{mol.L}^{-1}$ , respectively) were added and let in contact for 24  
20 h. The cells were washed with phosphate buffer (5 mL), and fixed in phosphate buffer  $1 \mu\text{mol.L}^{-1}$   
21 containing 1.6 % glutaraldehyde for 1 h at 4°C. They were washed with  $0.1 \text{ mol.L}^{-1}$  phosphate  
22 buffer at pH 7.2 (0.5 mL) and post-fixed in 1 % osmium tetroxide and cacodylate buffer for 1h  
23 at 4 °C. After fixation, the samples were rinsed with cacodylate buffer and dried with increasing  
24 concentrations of ethanol and propylene oxide, embedded in EMBed-812 resin (Agar Scientific,  
25 UK) and further polymerized. The resulting embedded cells were cut with an UltraCut E  
26 microtome (Leica, Wetzlar, Germany) and placed onto copper grids. TEM observation of grids  
27 was performed using a JEM-1010 microscope (JEOL, Tokyo, Japan), operating at an accelerated  
28 voltage of 100 kV.  
29  
30  
31  
32  
33  
34  
35  
36  
37  
38  
39  
40  
41  
42  
43  
44  
45

46 *Confocal fluorescence and transmission microscopy.* Confocal fluorescence imaging was  
47 performed using a Nikon A1R Si microscope, equipped with Ar<sup>+</sup> and He-Ne lasers as excitation  
48 sources and an oil-immersion objective Plan Apo, 60×, NA = 1.4). Transmission imaging were  
49 obtained using an Axio Observer.Z1 Zeiss microscope using two distinct objectives (oil-  
50 immersion objective: A Pln, 63×, NA = 1.4, DICIII; objective A Pln 40×, 0.5 Ph<sub>2</sub>). Cell imaging:  
51  
52  
53  
54  
55  
56  
57  
58  
59  
60

1  
2  
3 Meso 11 cells were seeded on a  $\mu$ -slide 8-well ibitreat microscopy chamber (Ibidi). After 24 h,  
4 solutions of **NA-1**, **NA-2** and **NA-3** (final iron concentration of  $3.3 \mu\text{mol.L}^{-1}$ ,  $2.6 \mu\text{mol.L}^{-1}$  and  
5  $2.09 \mu\text{mol.L}^{-1}$ , respectively) were added and let in contact for 24 h. Each well was washed with  
6 PBS and incubated with  $5 \mu\text{g.mL}^{-1}$  WGA Alexa Fluor® 647 conjugate for 10 min at  $37^\circ\text{C}$ . The  
7 cells were then washed twice with PBS and incubated with  $5 \mu\text{g.mL}^{-1}$  Hoechst for nucleus  
8 staining and 4 % paraformaldehyde for 15 minutes. Spheroid imaging: Meso 11 spheroids were  
9 treated with **NA-1**, **NA-2** and **NA-3** (final iron concentration of  $65.7 \mu\text{mol.L}^{-1}$ ,  $52.2 \mu\text{mol.L}^{-1}$  and  
10  $41.7 \mu\text{mol.L}^{-1}$ , respectively) for 24 h. Each well was washed with PBS and incubated with  $5$   
11  $\mu\text{g.mL}^{-1}$  Hoechst for nucleus staining and 4 % paraformaldehyde for 15 minutes. Meso 11 MTCS  
12 were washed once with PBS and transferred into  $\mu$ -slide angiogenesis plate (Ibidi) for imaging.

13  
14  
15  
16  
17  
18  
19  
20  
21  
22  
23  
24  
25  
26  
27 *Magnetic resonance imaging of cell monolayers and spheroids.* A scaffold was designed  
28 according to a glass cylinder ( $54 \text{ mm} \times 27 \text{ mm}$ ). The ghost background was filled by 1% low-  
29 melting agarose gel (type I - Sigma-Aldrich) and two rows of four wells were created thanks to a  
30 plastic comb designed by a 3D printer. Monolayers of Meso 11 cells were seeded in the first  
31 row's wells at a density of  $2 \times 10^4$  cells/well in PBS. Sixteen Meso 11 MTCS were seeded on  
32 each second row's well. The top of the scaffold was filled by 1 % low-gelling agarose gel (type I  
33 - Sigma-Aldrich). All MRI studies were performed with a Biospec Avance III MR scanner  
34 (Bruker Biospin, Wissembourg, France) using a 20 cm bore 7 T magnet equipped with BGA12S  
35 gradient/ shim system capable of  $675 \text{ mT.m}^{-1}$  maximum gradient strength. A 35-mm-diameter  
36 volume coil was used.

## 37 38 39 40 41 42 43 44 45 46 47 48 49 50 51 **ASSOCIATED CONTENT** 52 53 54 55 56 57 58 59 60

1  
2  
3 **Supporting Information.** SDS-PAGE and magnetophoresis protocols and additional TEM,  
4 photophysical and MRI characterizations. This material is available free of charge via the  
5 Internet at <http://pubs.acs.org>.  
6  
7  
8  
9

## 10 11 12 13 **AUTHOR INFORMATION**

### 14 15 **Corresponding Author**

16  
17 \*E-mail: elena.ishow@univ-nantes.fr – Phone: +33-2-5112-5375.

18  
19 \*E-mail: christophe.blanquart@univ-nantes.fr – Phone: +33-2-2808-0238.

20  
21 \*E-mail : julien.poly@uha.fr – Phone: +33-3-8960-8802.  
22  
23

### 24 25 **Author Contributions**

26  
27 The manuscript was written through contributions of all authors. All authors have given approval  
28 to the final version of the manuscript.  
29  
30  
31  
32

### 33 34 **Funding Sources**

35  
36 The “Ligue contre le cancer 44” is gratefully acknowledged for their strong support as well as  
37 CNRS through its “Mission pour l’Interdisciplinarité” board (program “Nano Challenge: Health  
38 and Welfare” / ETHICAM project) and its France-Italy partnership (program PICS /  
39 MOCACINO project), and Région des Pays de la Loire through the PhD program of  
40 LUMOMAT RFI (ONASSIS project).  
41  
42  
43  
44  
45  
46  
47  
48

## 49 50 **ACKNOWLEDGEMENT**

51  
52 We deeply acknowledge Carole La (LPGN, UMR CNRS 6112 – Université Nantes), Brigitte  
53 Bouchet (INRA Nantes-Angers), and Eric Gautron (IMN, UMR 6502 – Université Nantes), Louis  
54 Ryo and François-Xavier Lefèvre (CEISAM, UMR CNRS 6230 – Université Nantes), Florence  
55  
56  
57  
58  
59  
60

1  
2  
3 Franconi (PIAM- Angers), Thierry Guizouarn (ISCR, UMR CNRS 6226 – Université de Rennes  
4 1), Juliette Desfrancois (Plateforme CytoCell, INSERM UMR 1232, Nantes), Florence Gazeau  
5 and Claire Wilhelm (MSC, UMR CNRS 7057 – Université Paris Diderot), Jérôme Fresnais  
6 (PHENIX, UMR CNRS 8234 - Université Pierre et Marie Curie), for ICP-OES iron titrations,  
7 access to TEM platform, glass blowing and SEM measurements, MRI measurements, SQUID  
8 measurements, flow cytometry, access to magnetophoresis facilities, and for providing acidic  
9 solutions of SPIONs, respectively.  
10  
11  
12  
13  
14  
15  
16  
17  
18  
19  
20  
21

## 22 REFERENCES

- 23  
24 (1) Prado, Y.; Daffe, N.; Michel, A.; Georgelin, T.; Yaacoub, N.; Greneche, J.-M.;  
25 Choueikani, F.; Otero, E.; Ohresser, P.; Arrio, M.-A.; Cartier-dit-Moulin, C.; Saintavit, P.;  
26 Fleury, B.; Dupuis, V.; Lisnard, L.; Fresnais, J. Enhancing the magnetic anisotropy of  
27 maghemite nanoparticles via the surface coordination of molecular complexes. *Nat*  
28 *Commun* **2015**, *6*.  
29  
30 (2) de Boer, P.; Hoogenboom, J. P.; Giepmans, B. N. G. Correlated Light and Electron  
31 Microscopy: Ultrastructure Lights Up! *Nat. Methods* **2015**, *12*, 503-513.  
32  
33 (3) Feld, A.; Merkl, J.-P.; Kloust, H.; Flessau, S.; Schmidtke, C.; Wolter, C.; Ostermann, J.;  
34 Kampfbeck, M.; Eggers, R.; Mews, A.; Schotten, T.; Weller, H. A Universal Approach  
35 to Ultrasmall Magneto-Fluorescent Nanohybrids. *Angew. Chem., Int. Ed.* **2015**, *54*, 12468-  
36 12471.  
37  
38 (4) Chen, O.; Riedemann, L.; Etoc, F.; Herrmann, H.; Coppey, M.; Barch, M.; Farrar, C. T.;  
39 Zhao, J.; Bruns, O. T.; Wei, H.; Guo, P.; Cui, J.; Jensen, R.; Chen, Y.; Harris, D. K.;  
40 Cordero, J. M.; Wang, Z. W.; Jasanoff, A.; Fukumura, D.; Reimer, R.; Dahan, M.; Jain, R.  
41  
42  
43  
44  
45  
46  
47  
48  
49  
50  
51  
52  
53  
54  
55  
56  
57  
58  
59  
60

- 1  
2  
3 K.; Bawendi, M. G. Magneto-Fluorescent Core-Shell Supernanoparticles. *Nat. Commun.*  
4  
5 **2014**, *5*, 5093.  
6  
7  
8 (5) Reddy, L. H.; Arias, J. L.; Nicolas, J.; Couvreur, P. Magnetic Nanoparticles: Design and  
9  
10 Characterization, Toxicity and Biocompatibility, Pharmaceutical and Biomedical  
11  
12 Applications. *Chem. Rev.* **2012**, *112*, 5818-5878.  
13  
14  
15 (6) Mazuel, F.; Espinosa, A.; Luciani, N.; Reffay, M.; Le Borgne, R.; Motte, L.; Desboeufs,  
16  
17 K.; Michel, A.; Pellegrino, T.; Lalatonne, Y.; Wilhelm, C. Massive Intracellular  
18  
19 Biodegradation of Iron Oxide Nanoparticles Evidenced Magnetically at Single-Endosome  
20  
21 and Tissue Levels. *ACS Nano* **2016**, *10*, 7627-7638.  
22  
23  
24 (7) Lartigue, L.; Alloyeau, D.; Kolosnjaj-Tabi, J.; Javed, Y.; Guardia, P.; Riedinger, A.;  
25  
26 P  choux, C.; Pellegrino, T.; Wilhelm, C.; Gazeau, F. Biodegradation of Iron Oxide  
27  
28 Nanocubes: High-Resolution In Situ Monitoring. *ACS Nano* **2013**, *7*, 3939-3952.  
29  
30  
31 (8) Gupta, A. K.; Gupta, M. Synthesis and Surface Engineering of Iron Oxide Nanoparticles  
32  
33 for Biomedical Applications. *Biomaterials* **2005**, *26*, 3995-4021.  
34  
35  
36 (9) Lee, P.-W.; Hsu, S.-H.; Wang, J.-J.; Tsai, J.-S.; Lin, K.-J.; Wey, S.-P.; F.-R., C.; Lai, C.-  
37  
38 H.; Yen, T.-C.; Sung, H.-W. The Characteristics, Biodistribution, Magnetic Resonance  
39  
40 Imaging and Biodegradability of Superparamagnetic Core-Shell Nanoparticles.  
41  
42 *Biomaterials* **2010**, *1316-1324*, 1316-1324.  
43  
44  
45 (10) Laurent, S.; Forge, D.; Port, M.; Roch, A.; Robic, C.; Vander Elst, L.; Muller, R. N.  
46  
47 Magnetic Iron Oxide Nanoparticles: Synthesis, Stabilization, Vectorization,  
48  
49 Physicochemical Characterizations, and Biological Applications. *Chem. Rev.* **2008**, *108*,  
50  
51 2064-2110.  
52  
53  
54  
55  
56  
57  
58  
59  
60

- 1  
2  
3 (11) Vuong, Q. L.; Berret, J. F.; Fresnais, J.; Gossuin, Y.; Sandre, O. A Universal Scaling Law  
4 to Predict the Efficiency of Magnetic Nanoparticles as MRI T2-Contrast Agents. *Adv.*  
5 *Healthcare Mater.* **2012**, *1*, 502-512.  
6  
7  
8  
9  
10 (12) Paquet, C.; de Haan, H. W.; Leek, D. M.; Lin, H. Y.; Xiang, B.; Tian, G. H.; Kell, A.;  
11 Simard, B. Clusters of Superparamagnetic Iron Oxide Nanoparticles Encapsulated in a  
12 Hydrogel: A Particle Architecture Generating a Synergistic Enhancement of the T-2  
13 Relaxation. *ACS Nano* **2011**, *5*, 3104-3112.  
14  
15  
16  
17  
18 (13) Hickey, R. J.; Koski, J.; Meng, X.; Riggleman, R. A.; Zhang, P. J.; Park, S. J. Size-  
19 Controlled Self-Assembly of Superparamagnetic Polymersomes. *ACS Nano* **2014**, *8*, 495-  
20 502.  
21  
22  
23  
24  
25  
26 (14) Béalle, G.; Di Corato, R.; Kolosnjaj-Tabi, J.; Dupuis, V.; Clément, O.; Gazeau, F.;  
27 Wilhelm, C.; Ménager, C. Ultra Magnetic Liposomes for MR Imaging, Targeting, and  
28 Hyperthermia. *Langmuir* **2012**, *28*, 11834-11842.  
29  
30  
31  
32  
33 (15) Casula, M. F.; Floris, P.; Innocenti, C.; Lascialfari, A.; Marinone, M.; Corti, M.; Sperling,  
34 R. A.; Parak, W. J.; Sangregorio, C. Magnetic Resonance Imaging Contrast Agents Based  
35 on Iron Oxide Superparamagnetic Ferrofluids. *Chem. Mater.* **2010**, *22*, 1739-1748.  
36  
37  
38  
39 (16) Di Corato, R.; Béalle, G.; Kolosnjaj-Tabi, J.; Espinosa, A.; Clément, O.; Silva, A. K. A.;  
40 Ménager, C.; Wilhelm, C. Combining Magnetic Hyperthermia and Photodynamic Therapy  
41 for Tumor Ablation with Photoresponsive Magnetic Liposomes. *ACS Nano* **2015**, *9*, 2904-  
42 2916.  
43  
44  
45  
46  
47  
48  
49 (17) Faucon, A.; Fresnais, J.; Brosseau, A.; Hulin, P.; Nedellec, S.; Hemez, J.; Ishow, E.  
50 Photoactive Chelating Organic Nanospheres as Central Platforms of Bimodal Hybrid  
51 Nanoparticles. *J. Mater. Chem. C* **2013**, *1*, 3879-3886.  
52  
53  
54  
55  
56  
57  
58  
59  
60

- 1  
2  
3  
4  
5  
6  
7  
8  
9  
10  
11  
12  
13  
14  
15  
16  
17  
18  
19  
20  
21  
22  
23  
24  
25  
26  
27  
28  
29  
30  
31  
32  
33  
34  
35  
36  
37  
38  
39  
40  
41  
42  
43  
44  
45  
46  
47  
48  
49  
50  
51  
52  
53  
54  
55  
56  
57  
58  
59  
60
- (18) Faucon, A.; Benhelli-Mokran, H.; Fleury, F.; Dubreil, L.; Hulin, P.; Nedellec, S.; Doussineau, T.; Antoine, R.; Orlando, T.; Lascialfari, A.; Fresnais, J.; Lartigue, L.; Ishow, E. Tuning the Architectural Integrity of High-Performance Magnetofluorescent Core-Shell Nanoassemblies in Cancer Cells. *J. Colloid Interface Sci.* **2016**, *479*, 139–149.
- (19) Fresnais, J.; Berret, J.-F.; Frka-Petesic, B.; Sandre, O.; Perzynski, R. Electrostatic Co-Assembly of Iron Oxide Nanoparticles and Polymers: Towards the Generation of Highly Persistent Superparamagnetic Nanorods. *Adv. Mater.* **2008**, *20*, 1-5.
- (20) Chanteau, B.; Fresnais, J.; Berret, J. F. Electrosteric Enhanced Stability of Functional Sub-10 nm Cerium and Iron Oxide Particles in Cell Culture Medium. *Langmuir* **2009**, *25*, 9064-9070.
- (21) Kadajji, V. G.; Betageri, G. V. Water Soluble Polymers for Pharmaceutical Applications. *Polymers* **2011**, *2*, 1972-2009.
- (22) Faucon, A.; Maldiney, T.; Clément, O.; Hulin, P.; Nedellec, S.; Robard, M.; Gautier, N.; De Meulenaere, E.; Clays, K.; Orlando, T.; Lascialfari, A.; Fiorini-Debuisschert, C.; Fresnais, J.; Ishow, E. Highly Cohesive Dual Nanoassemblies for Complementary Multiscale Bioimaging. *J. Mater. Chem. B* **2014**, *2*, 7747-7755.
- (23) Torrisi, V.; Graillet, A.; Vitorazi, L.; Crouzet, Q.; Marletta, G.; Loubat, C.; Berret, J. F. Preventing Corona Effects: Multiphosponic Acid Poly(ethylene glycol) Copolymers for Stable Stealth Iron Oxide Nanoparticles. *Biomacromolecules* **2014**, *15*, 3171-3179.
- (24) Markiewicz, K. H.; Seiler, L.; Misztalewska, I.; Winkler, K.; Harrison, S.; Wilczewska, A. Z.; Destarac, M.; Marty, J. D. Advantages of Poly(Vinyl Phosphonic Acid)-Based Double Hydrophilic Block Copolymers for The Stabilization of Iron Oxide Nanoparticles. *Polymer Chem.* **2016**, *7*, 6391-6399.

- 1  
2  
3 (25) Verma, A.; Stellacci, F. Effect of surface properties on nanoparticle-cell interactions. *Small*  
4  
5 **2010**, *6*, 12-21.  
6  
7  
8 (26) Ashby, J.; Pan, S. Q.; Zhong, W. W. Size and Surface Functionalization of Iron Oxide  
9  
10 Nanoparticles Influence the Composition and Dynamic Nature of Their Protein Corona.  
11  
12 *ACS Appl. Mater. Interfaces* **2014**, *6*, 15412-15419.  
13  
14  
15 (27) Saha, K.; Rahimi, M.; Yazdani, M.; Kim, S. T.; Moyano, D. F.; Hou, S.; Das, R.; Mout, R.;  
16  
17 Rezaee, F.; Mahmoudi, M.; Rotello, V. M. Regulation of Macrophage Recognition through  
18  
19 the Interplay of Nanoparticle Surface Functionality and Protein Corona. *ACS Nano* **2016**,  
20  
21 *10*, 4421-4430.  
22  
23  
24 (28) Huang, R.; Carney, R. P.; Ikuma, K.; Stellacci, F.; Lau, B. L. T. Effects of Surface  
25  
26 Compositional and Structural Heterogeneity on Nanoparticle-Protein Interactions:  
27  
28 Different Protein Configurations. *ACS Nano* **2014**, *8*, 5402-5412.  
29  
30  
31 (29) Nasongkla, N.; Chen, B.; Macaraeg, N.; Fox, M. E.; Fréchet, J. M. J.; Szoka, F. C.  
32  
33 Dependence of Pharmacokinetics and Biodistribution on Polymer Architecture: Effect of  
34  
35 Cyclic versus Linear Polymers. *J. Am. Chem. Soc.* **2009**, *131*, 3842-3843.  
36  
37  
38 (30) Setyawati, M. I.; Tay, C. Y.; Docter, D.; Stauber, R. H.; Leong, D. T. Understanding and  
39  
40 Exploiting Nanoparticles' Intimacy with The Blood Vessel and Blood. *Chem. Soc. Rev.*  
41  
42 **2015**, *44*.  
43  
44  
45 (31) Ménager, C.; Sandre, O.; Mangili, J.; Cabuil, V. Preparation and Swelling of Hydrophilic  
46  
47 Magnetic Microgels. *Polymer* **2004**, *45*, 2475-2481.  
48  
49  
50 (32) Fery-Forgues, S. Fluorescent organic nanocrystals and non-doped particles for biological  
51  
52 applications. *Nanoscale* **2013**, *51*, 8428-8437.  
53  
54  
55  
56  
57  
58  
59  
60

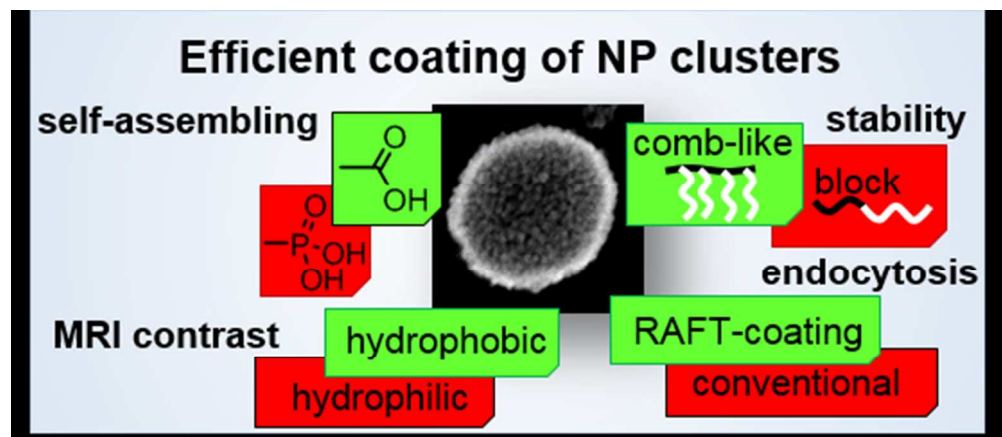
- 1  
2  
3  
4  
5  
6  
7  
8  
9  
10  
11  
12  
13  
14  
15  
16  
17  
18  
19  
20  
21  
22  
23  
24  
25  
26  
27  
28  
29  
30  
31  
32  
33  
34  
35  
36  
37  
38  
39  
40  
41  
42  
43  
44  
45  
46  
47  
48  
49  
50  
51  
52  
53  
54  
55  
56  
57  
58  
59  
60
- (33) Fischer, I.; Petkau-Milroy, K.; Dorland, Y. L.; Schenning, A.; Brunsveld, L. Self-Assembled Fluorescent Organic Nanoparticles for Live-Cell Imaging. *Chem. Eur. J.* **2013**, *19*, 16646-16650.
- (34) Bouhamed, H.; Boufi, S.; Magnin, A. Alumina interaction with AMPS-MPEG copolymers produced by RAFT polymerization: Stability and rheological behavior. *J. Coll. Interface Sci.* **2009**, *333*, 209-220.
- (35) McCormick, C. L.; Lowe, A. B. Aqueous RAFT Polymerization: Recent Developments in Synthesis of Functional Water-Soluble (Co)polymers with Controlled Structures. *Acc. Chem. Res.* **2004**, *37*, 312-325.
- (36) Boyer, C.; Bulmus, V.; Davis, T. P.; Ladmiral, V.; Liu, J.; Perrier, S. Bioapplications of RAFT Polymerization. *Chem. Rev.* **2009**, *109*, 5402-5436.
- (37) Tian, J.; Zheng, F.; Zhao, H. Nanoparticles with Fe<sub>3</sub>O<sub>4</sub>-Nanoparticle Cores and Gold-Nanoparticle Coronae Prepared by Self-Assembly Approach. *The Journal of Physical Chemistry C* **2011**, *115*, 3304-3312.
- (38) Pissuwan, D.; Boyer, C.; Gunasekaran, K.; Davis, T. P.; Bulmus, V. In Vitro Cytotoxicity of RAFT Polymers. *Biomacromolecules* **2010**, *11*, 412-420.
- (39) Sumerlin, B. S.; Matyjaszewski, K., Molecular Brushes – Densely Grafted Copolymers. In *Macromolecular Engineering*, Wiley-VCH Verlag GmbH & Co. KGaA: 2007; pp 1103-1135.
- (40) Mignot, A.; Truillet, C.; Lux, F.; Sancey, L.; Louis, C.; Denat, F.; Boschetti, F.; Bocher, L.; Gloter, A.; Stephan, O.; Antoine, R.; Dugourd, P.; Luneau, D.; Novitchi, G.; Figueiredo, L. C.; de Morais, P. C.; Bonneviot, L.; Albela, B.; Ribot, F.; Van Lokeren, L.; Dechamps-Olivier, I.; Chuburu, F.; Lemerrier, G.; Villiers, C.; Marche, P. N.; Le Duc, G.;

- 1  
2  
3 Roux, S.; Tillement, O.; Perriat, P. A Top-Down Synthesis Route to Ultrasmall  
4 Multifunctional Gd-Based Silica Nanoparticles for Theranostic Applications. *Chem. Eur. J.*  
5  
6 **2013**, *19*, 6122-6136.  
7  
8  
9
- 10 (41) Ishow, E.; Faucon, A. Magnetic and Fluorescent Reverse Nanoassemblies. US 14/218,368  
11  
12 - PCT/EP2015/055711, **March 2015**.  
13  
14
- 15 (42) Johnson, N. J. J.; He, S.; Hun, V. A. N.; Almutairi, A. Compact Micellization: A Strategy  
16  
17 for Ultrahigh T-1 Magnetic Resonance Contrast with Gadolinium-Based Nanocrystals.  
18  
19 *ACS Nano* **2016**, *10*, 8299-8307.  
20  
21
- 22 (43) Willcock, H.; K. O'Reilly, R. End Group Removal and Modification of RAFT Polymers.  
23  
24 *Polym. Chem.* **2010**, *1*, 149-157.  
25  
26
- 27 (44) Faucon, A.; Lenk, R.; Hemez, J.; Gautron, E.; Jacquemin, D.; Le Questel, J.-Y.; Graton, J.;  
28  
29 Brosseau, A.; Ishow, E. Fluorescent Carboxylic and Phosphonic Acids: Comparative  
30  
31 Photophysics from Solution to Organic Nanoparticles. *Phys. Chem. Chem. Phys.* **2013**, *15*,  
32  
33 12748-12756.  
34  
35
- 36 (45) Faucon, A.; Benhelli-Mokrani, H.; Córdova, L. A.; Brulin, B.; Heymann, D.; Hulin, P.;  
37  
38 Nedellec, S.; Ishow, E. Long-Term Fate of Fluorescent Organic Nanoparticles as  
39  
40 Bioimaging Agents in Cancer Cells and Macrophages. *Adv. Health. Mater* **2015**, *4*, 2727-  
41  
42 2734.  
43  
44
- 45 (46) Breton, M.; Prevel, G.; Audibert, J. F.; Pansu, R.; Tauc, P.; Le Pioufle, B.; Francais, O.;  
46  
47 Fresnais, J.; Berret, J. F.; Ishow, E. Solvatochromic Dissociation of Non-Covalent  
48  
49 Fluorescent Organic Nanoparticles upon Cell Internalization. *Phys. Chem. Chem. Phys.*  
50  
51 **2011**, *13*, 13268-13276.  
52  
53  
54  
55  
56  
57  
58  
59  
60

- 1  
2  
3  
4  
5  
6  
7  
8  
9  
10  
11  
12  
13  
14  
15  
16  
17  
18  
19  
20  
21  
22  
23  
24  
25  
26  
27  
28  
29  
30  
31  
32  
33  
34  
35  
36  
37  
38  
39  
40  
41  
42  
43  
44  
45  
46  
47  
48  
49  
50  
51  
52  
53  
54  
55  
56  
57  
58  
59  
60
- (47) Farinha, J. P. S.; Relógio, P.; Charreyre, M.-T.; Prazeres, T. J. V.; Martinho, J. M. G. Understanding Fluorescence Quenching in Polymers Obtained by RAFT. *Macromolecules* **2007**, *40*, 4680-4690.
- (48) Nandwana, V.; Ryoo, S. R.; Kanthala, S.; De, M.; Chou, S. S.; Prasad, P. V.; Dravid, V. P. Engineered Theranostic Magnetic Nanostructures: Role of Composition and Surface Coating on Magnetic Resonance Imaging Contrast and Thermal Activation. *ACS Appl. Mater. Interfaces* **2016**, *8*, 6953-6961.
- (49) Poselt, E.; Kloust, H.; Tromsdorf, U.; Janschel, M.; Hahn, C.; Masslo, C.; Weller, H. Relaxivity Optimization of a PEGylated Iron-Oxide-Based Negative Magnetic Resonance Contrast Agent for T-2-Weighted Spin-Echo Imaging. *ACS Nano* **2012**, *6*, 1619-1624.
- (50) Roch, A.; Muller, R. N.; Gillis, P. Theory of Proton Relaxation Induced by Superparamagnetic Particles. *J. Chem. Phys.* **1999**, *110*, 5403-5411.
- (51) Ternent, L.; Mayoh, D. A.; Lees, M. R.; Davies, G. L. Heparin-Stabilised Iron Oxide for MR Applications: A Relaxometric Study. *J. Mater. Chem. B* **2016**, *4*, 3065-3074.
- (52) Meledandri, C. J.; Ninjbadgar, T.; Brougham, D. F. Size-controlled magnetoliposomes with tunable magnetic resonance relaxation enhancements. *J. Mater. Chem.* **2011**, *21*, 214-222.
- (53) Gossuin, Y.; Gillis, P.; Hocq, A.; Vuong, Q. L.; Roch, A. Magnetic Resonance Relaxation Properties of Superparamagnetic Particles. *Wiley Interdiscip. Rev.: Nanomed. Nanobiotechnol.* **2009**, *1*, 299-310.
- (54) Vuong, Q. L.; Berret, J.-F.; Fresnais, J.; Gossuin, Y.; Sandre, O. A Universal Scaling Law to Predict the Efficiency of Magnetic Nanoparticles as MRI T2-Contrast Agents. *Adv. Health. Mater.* **2012**, *1*, 502-512.

- 1  
2  
3 (55) Meng, H.; Xia, T.; George, S.; Nel, A. E. A Predictive Toxicological Paradigm for the  
4 Safety Assessment of Nanomaterials. *ACS Nano* **2009**, *3*, 1620-1627.  
5  
6  
7  
8 (56) Lartigue, L.; Hugounenq, P.; Alloyeau, D.; Clarke, S. P.; Lévy, M.; Bacri, J.-C.; Bazzi, R.;  
9 Brougham, D. F.; Wilhelm, C.; Gazeau, F. Cooperative Organization in Iron Oxide Multi-  
10 Core Nanoparticles Potentiates Their Efficiency as Heating Mediators and MRI Contrast  
11 Agents. *ACS Nano* **2012**, *6*, 10935-10949.  
12  
13  
14  
15  
16  
17 (57) Jansch, M.; Stumpf, P.; Graf, C.; Rühl, E.; Müller, R. H. Adsorption Kinetics of Plasma  
18 Proteins on Ultrasmall Superparamagnetic Iron Oxide (USPIO) Nanoparticles. *Int. J.*  
19 *Pharm.* **2012**, *428*, 125-133.  
20  
21  
22  
23  
24 (58) Xia, T.; Kovochich, M.; Liong, M.; Zink, J. I.; Nel, A. E. Cationic Polystyrene Nanosphere  
25 Toxicity Depends on Cell-Specific Endocytic and Mitochondrial Injury Pathways. *ACS*  
26 *Nano* **2008**, *2*, 85-96.  
27  
28  
29  
30  
31 (59) Weinstein, J. S.; Varallyay, C. G.; Dosa, E.; Gahramanov, S.; Hamilton, B.; Rooney, W.  
32 D.; Muldoon, L. L.; Neuwelt, E. A. Superparamagnetic iron oxide nanoparticles:  
33 diagnostic magnetic resonance imaging and potential therapeutic applications in  
34 neurooncology and central nervous system inflammatory pathologies, a review. *J. Cereb.*  
35 *Blood Flow Metab.* **2010**, *30*, 15-35.  
36  
37  
38  
39  
40  
41  
42  
43 (60) Wrynna, A. S.; Mac Sweeney, C. I. P.; Franconi, F.; Lemaire, L.; Pouliquen, D.;  
44 Herlidou, S.; Leonard, B. E.; Gandon, J.-M.; de Certaines, J. D. An In-Vivo Magnetic  
45 Resonance Imaging Study of The Olfactory Bulbectomized Rat Model of Depression.  
46 *Brain Res.* **2000**, *879*, 193-199.  
47  
48  
49  
50  
51  
52  
53  
54  
55  
56  
57  
58  
59  
60

- 1  
2  
3  
4  
5  
6  
7  
8  
9  
10  
11  
12  
13  
14  
15  
16  
17  
18  
19  
20  
21  
22  
23  
24  
25  
26  
27  
28  
29  
30  
31  
32  
33  
34  
35  
36  
37  
38  
39  
40  
41  
42  
43  
44  
45  
46  
47  
48  
49  
50  
51  
52  
53  
54  
55  
56  
57  
58  
59  
60
- (61) Tanimoto, A. T.; Pouliquen, D.; Kreft, B. P.; Stark, D. D. Effects of Spatial Distribution on Proton Relaxation Enhancement by Particulate Iron Oxide. *J. Magn. Reson. Imaging* **1994**, *4*, 653-657.
- (62) Weiswald, L.-B.; Bellet, D.; Dangles-Marie, V. Spherical Cancer Models in Tumor Biology. *Neoplasia* **2015**, *17*, 1-15.
- (63) Fennema, E.; Rivron, N.; Rouwkema, J.; van Blitterswijk, C.; de Boer, J. Spheroid Culture as A Tool for Creating 3D Complex Tissues. *Trends Biotechnol.* **2012**, *31*, 108-115.
- (64) Levy, M. L., F.; Maraloiu, V. A.; Blanchin, M. G.; Gendron, F.; Wilhelm, C.; Gazeau, F. Degradability of Superparamagnetic Nanoparticles in a Model of Intracellular Environment: Follow-up of Magnetic, Structural and Chemical Properties. *Nanotechnology* **2010**, *21*, 395103-395200.
- (65) Reynolds, L.; Gardecki, J. A.; Frankland, S. J. V.; Horng, M. L.; Maroncelli, M. Dipole Solvation in Nondipolar Solvents: Experimental Studies of Reorganization Energies and Solvation Dynamics. *J. Phys. Chem. C* **1996**, *100*, 10337-10354.



94x40mm (150 x 150 DPI)